THE MOBILITY OF DISLOCATIONS
IN HIGH PURITY ALUMINUM

Thesis by

Jeffrey Archibald Gorman

In Partial Fulfillment of the Requirements
For the Degree of
Doctor of Philosophy

California Institute of Technology
Pasadena, California
1968

(Submitted May 14, 1968)

ACKNOWLEDGEMENTS

The author wishes to thank Professor D. S. Wood for his continued interest and encouragement during the course of this work, and to thank Professor T. Vreeland, Jr. for his many helpful suggestions and comments. Appreciation is extended to Professor N. George for his encouragement and help in applying the laser to this work. Thanks are also expressed to Mr. G. R. May for his assistance in specimen preparation.

The author acknowledges support by the United States Atomic Energy Commission by the award of a special fellowship in nuclear science and engineering administered by Oak Ridge Associated Universities. The research was performed under a contract with the United States Atomic Energy Commission.

The author especially thanks his wife, Ginni, for her patience, understanding, and encouragement during the performance of this work.

ABSTRACT

This thesis presents the results of measurements of the velocities of edge and mixed dislocations in aluminum as a function of temperature and applied shear stress. All tests were conducted on 99.999% purity aluminum single crystals. Dislocation velocities were determined by observing the positions of dislocations by the Berg-Barrett X-ray technique before and after applying a stress pulse. Torsion stress pulses of microsecond duration were applied by propagating torsional waves along the axes of cylindrical crystals. Resolved shear stress up to 16 X 10^6 dynes/cm^2 were applied at temperatures from -150°C to 70°C. Measured dislocation velocities ranged from 10 to 2750 cm/sec. The velocities measured are believed to be characteristic of single straight dislocations moving through essentially perfect crystals, where the velocity is not significantly influenced by dislocation curvature, impurities or dislocation-dislocation interactions.

The results of this study indicate that the velocity of edge and mixed dislocations is linearly proportional to the applied resolved shear stress in the temperature range studied. Dislocation velocity increases as temperature is decreased. These results are compared to the predictions of theories which treat the interaction between moving dislocations and the lattice (phonon interactions). The theoretically predicted variation of dislocation velocity with temperature and stress agrees fairly well with the experimental results, but the predicted velocities are about six times less than the experimental velocities. Possible reasons for this discrepancy are discussed.

TABLE OF CONTENTS

TABLE OF CONTENTS--Continued

TABLE OF CONTENTS--Continued

LIST OF FIGURES

LIST OF FIGURES--Continued

I. INTRODUCTION

Dislocation dynamics attempts to predict the plastic deformation behavior of crystals by considering how dislocations move, multiply, and interact with other dislocations or other barriers to their motion. The basic equation governing the plastic behavior of crystals is

$$\dot{\gamma} = \rho_m b\bar{v} \qquad [1]$$

where $\dot{\gamma}$ is the plastic shear strain rate, ρ_m is the total length of moving dislocation line per unit volume hereafter called the density of mobile dislocations, b is the Burgers vector of the dislocations, and $\bar{v}$ is the average velocity of the mobile dislocations. Dislocation dynamics has been successful in explaining a number of plastic flow phenomena, for example Johnston and Gilman (1), who performed the first measurements of dislocation velocity, successfully predicted yield points in lithium floride. Transient creep (2), high velocity impact phenomena (3), and yield points and delay times in single crystals (4) have also been successfully explained using dislocation dynamics.

As shown by equation [1] the average velocity of mobile dislocations is an important parameter in describing the plastic flow of crystals. The average velocity of mobile dislocations is a function of many factors such as applied stress, temperature, internal stresses, impurities, etc. The starting point for understanding the average dislocation velocity is an understanding of how the velocity of individual dislocations varies in pure, perfect crystals as a function of

,tress and temperature. Once this is understood, attempts can be made to account for other factors such as impurities. In this thesis the velocity of dislocations in high purity, essentially perfect, single crystals of aluminum is studied.

Dislocation velocity has been measured by various direct and indirect methods. In the direct methods, individual dislocation positions are observed. In the indirect methods, dislocation velocity is deduced from measurements of the macroscopic behavior of a crystal using some assumed dislocation model. The indirect tests are in general easier to perform, but the results are uncertain because of possible errors in the assumed models. For example, internal friction measurements such as those for aluminum (5) provide data on the ratio ρ_m/B, where ρ_m is the density of mobile dislocations and B is a drag coefficient defined as the ratio of the applied force on a dislocation to its velocity. The density of mobile dislocations must be assumed in order to obtain a value for the drag coefficient. Strain rate tests are also difficult to interpret. In strain rate tests a step change in strain rate is imposed on a specimen and the instantaneous change in stress is measured. The change in strain rate as a function of the change in stress is then related to the variation in the velocity of dislocations as a function of stress by means of equation [1]. As discussed by Guard (6), changes in the density of mobile dislocations as strain rate is changed can confuse the interpretation of results.

Direct dislocation velocity measurements have been performed on a variety of materials using etch pit (1, 7-13) and X-ray techniques (8, 14, 15). In these measurements, dislocation position was determined before and after applying a stress pulse, and the velocity was deduced from the measured dislocation displacement and known duration of the stress pulse. These measurements have shown that dislocation velocity in covalently or ionically bonded materials and in metals with a BCC crystal structure is much less than one cm/sec at their flow stress. Also, dislocation velocity in these materials increases rapidly as temperature is increased. The low values and strong temperature dependence of the dislocation velocity indicate that the dislocation velocity is controlled by interactions with barriers which require thermal activation to be overcome, such as Peierls barriers (lattice forces in the perfect crystal) or lattice distortion due to impurities.

Direct dislocation velocity measurements have recently been performed for dislocations moving on close packed planes in HCP and FCC metals, high purity zinc (15, 16) and copper (10-12), and nickel with 80 ppm of carbon (9). These measurements indicate that dislocation velocity at the flow stress is much larger than one cm/sec in high purity zinc and copper, that the dislocation velocity is nearly linearly proportional to applied stress, and that dislocation velocity either decreases slowly with increases in temperature (16) or remains constant (11). This weak dependence on temperature is interpreted as meaning that thermal activation does not control dislocation motion on close packed planes in high purity FCC and HCP metals, but that some viscous damping mechanisms are involved. Various damping mechanisms have been proposed and will be discussed later in this thesis. The results obtained for nickel with 80 ppm dissolved carbon (9) indicate low dislocation velocity and strong temperature dependence of dislocation velocity. This behavior, typical of that for thermal activation controlled dislocation velocity, is attributed to the 80 ppm carbon dissolved in the nickel.

The strength of the viscous damping mechanisms controlling the velocity of dislocations on close packed planes of HCP and FCC metals may depend on the dislocation stacking fault width. Copper and aluminum are both FCC metals, but copper has a low stacking fault energy and thus a large dislocation stacking fault width, while aluminum has a high stacking fault energy and a low stacking fault width (17). Tests are underway (18) to determine the temperature dependence of dislocation velocity in copper. One of the purposes of this investigation of dislocation velocity in aluminum was to determine the stress and temperature dependence of dislocation velocity in a FCC metal with high stacking fault energy to provide a comparison with the behavior of dislocations in a material with low stacking fault energy.

II. TEST SPECIMEN PREPARATION

The test specimens used were single crystals of 99.999% pure aluminum machined into small right circular cylinders with the [111] direction along the cylindrical axis as shown in Figure 1. Test specimens were prepared by growing single crystals from which five or more specimens were machined. The machined specimens were then prepared for use by a cleaning and annealing treatment. A detailed description of the techniques used in test specimen preparation is given in the sections which follow.

Crystal Growth

Single aluminum crystals were grown using 99.999% pure aluminum which was supplied by Alfa Crystals, Division of Alfa Inorganics, Beverly, Massachusetts, by United Mineral and Chemical Corporation, New York, New York, and by Wilshire Chemical Company, Gardena, California. Satisfactory crystals were grown in high purity graphite molds under high vacuums (about 10^{-5} mm Hg) using a modified Bridgeman technique and a furnace similar to that described by Young (19). Grade AUC graphite supplied by the National Carbon Company, Division of Union Carbide, New York, New York was used. The mold was coated with 'dag' dispersion No. 154 (colloidal graphite in alcohol) supplied by Acheson Colloids Company, Port Huron, Michigan, and baked at 150°C in air before installing the aluminum charge in order to prevent bonding of the aluminum to the mold.

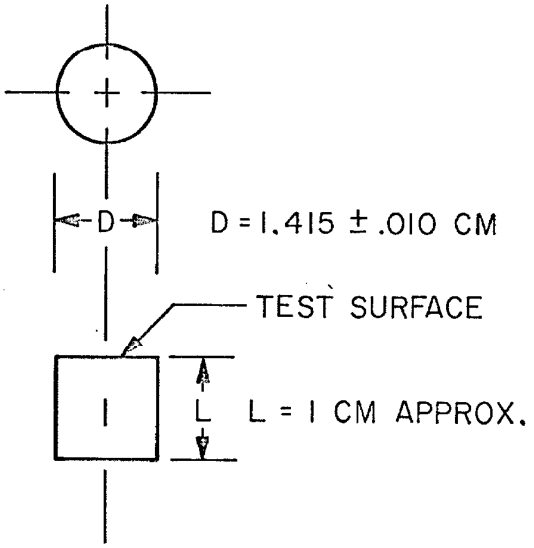

NOTES: 1. AXIS PARALLEL TO [111] WITHIN 2°
2. TEST SURFACE AND BOTTOM SURFACE PARALLEL TO (111) WITHIN 1/2°

Fig. 1. Test Specimen Geometry.

A satisfactory crystal was also grown by a soft mold technique similar to that described by Noggle (20), except that a helium atmosphere was used rather than high vacuum. It was necessary to bake the aluminum charge and alumina mold powder at 600°C under mechanical pump vacuum before growing the crystal. If the prior bake was not done, bubbles formed in the aluminum, apparently due to hydrogen picked up from water vapor attached to the alumina powder.

The best crystals produced in the graphite molds had subgrains of 3 or 4 millimeter diameters after a one hour anneal at 630°C. The crystals grown by the soft mold technique required about two weeks of annealing while cycling the temperature between 480°C and 635°C once an hour to obtain comparable subgrain sizes.

Specimen Machining

The as grown crystals were one inch in diameter and about six to ten inches long, and had a conical tip. The orientation of the crystallographic axes with respect to the macroscopic geometry of the crystal was determined using the Laue back reflection X-ray technique. Cylinders with a 1.78 cm diameter and with [111] axes were then trepanned using a spark discharge machine. A trepanned crystal, together with a trepanned [111] axis specimen, is shown in Figure 2. The ends of the specimen were then sawed off approximately perpendicular to the specimen axis using a spark discharge machine.

The specimen was mounted on a goniometer and the crystallographic orientation checked using the Laue back reflection technique with a

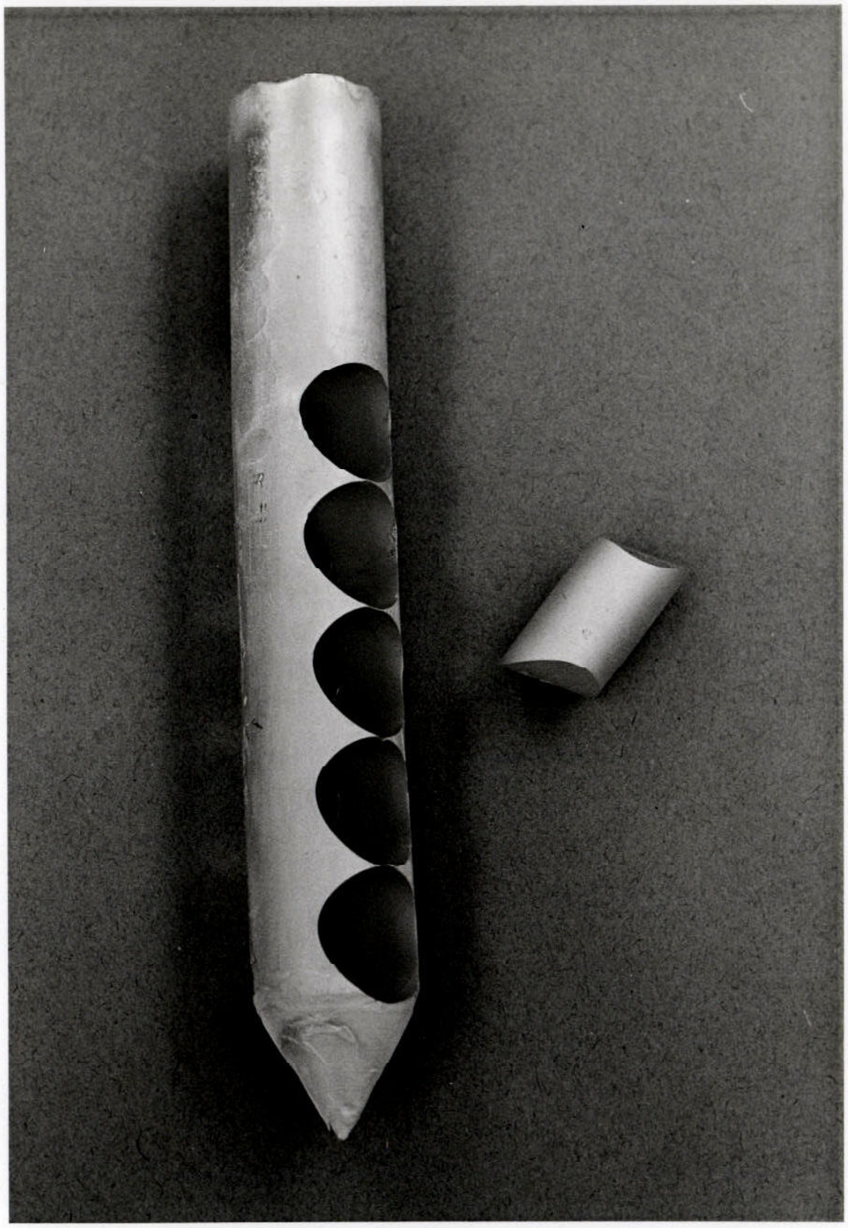

Fig. 2. Trepanned Crystal and [111] Axis Specimen.

5 cm specimen to film distance. One end of the specimen was spark planed perpendicular to the [111] direction. The specimen was then removed from the goniometer and the spark planed end was attached to a polycrystalline aluminum thermal buffer using an electrically conducting wax.

The specimen was machined to a final diameter of 1.415 + .008 cm using an electrolytic lathe. This machining removed all the material from the cylindrical surfaces which was damaged by spark machining. All electrolytic machining was done using an electrolyte of 2 parts methanol to 1 part nitric acid. The electrolytic lathe, illustrated in Figure 3a, consisted of a rotating bakelite wheel with a stainless steel rim covered by flannel cloth which served as the cathode. As the wheel turned, the cloth picked up electrolyte. The specimen was also rotated, and rested lightly on the flannel cloth covering the cathode.

The final step in the machining processes was to machine the end of the cylinder which would be the test surface shown in Figure 1. The specimen and thermal buffer were installed on a goniometer and aligned to within ± 1/2 degree using the Laue back reflection technique with a 5 cm specimen to film distance. At least 1 1/2 mm was then electrolytically machined off the end of the crystal using an electrolytic lap. The electrolytic lap, shown in Figure 3b, has a rotating stainless steel plate covered with flannel cloth as the cathode. The specimen, which was also rotating, bore lightly against the flannel

a. PHOTOGRAPH OF SPECIMEN IN LATHE

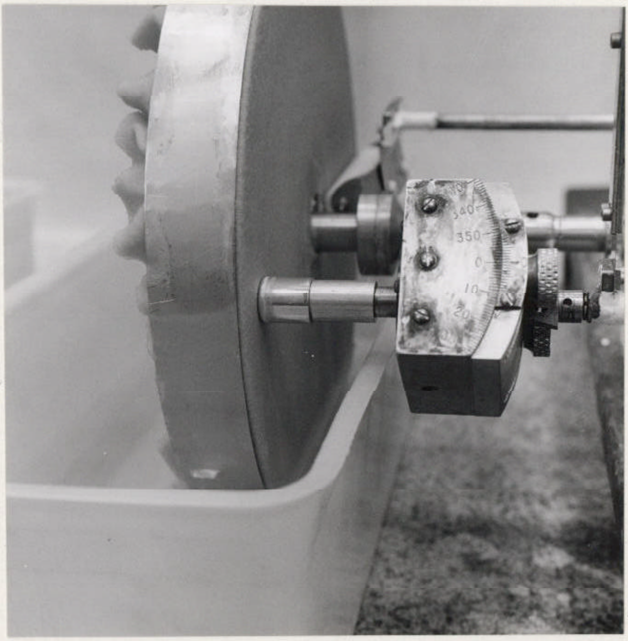

b. PHOTOGRAPH OF SPECIMEN IN LAP

Fig. 3. Electrolytic Machining Equipment.

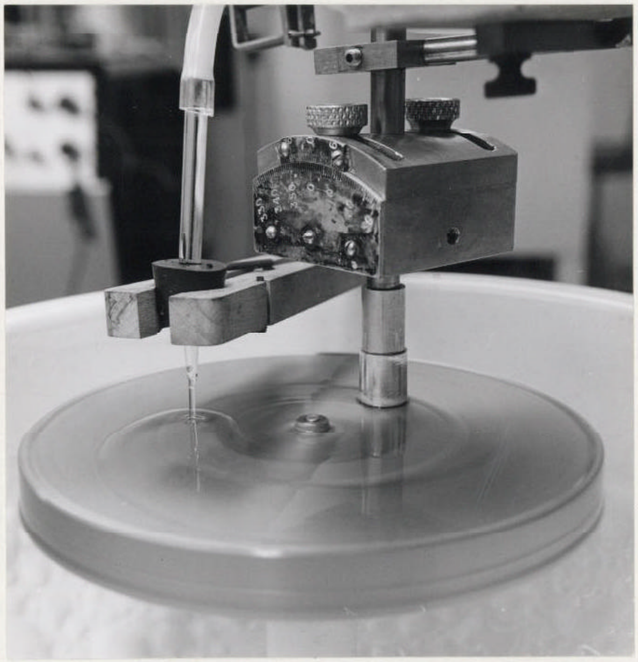

c. PHOTOGRAPH OF SPECIMEN IN FINAL POLISHING LAP

Fig. 3. continued

cloth. Finally, the specimen, still on the goniometer, was electrolytically machined for a few minutes using the final polishing lap shown in Figure 3c. This lap had a bare stainless steel plate rotating at high speed as the cathode. The specimen was held about .008 cm above the plate during machining, and was also rotated.

A current density of about 1 ampere/cm^2 was used for most of the electrolytic machining. If the surface had a thick oxide coating it was found useful to use a current density of about 5 ampere/cm^2 for the first fifteen seconds to break down the oxide coating uniformly over the surface.

Test specimens were used several times. After use, the specimen was mounted, aligned, and the test surface repolished using the same techniques as for new specimens.

Annealing

After final polishing the specimens were cleaned and annealed to remove stray bulk dislocations, that is, dislocations not a part of a subgrain boundary. A one hour anneal at 630°C was found to remove all stray bulk dislocations to a depth observable by the Berg-Barrett X-ray technique (about 10 microns).

Cleaning of the specimens before annealing consisted of the following steps:

1) Removing the mounting wax by washing in xylene at 65°C.

2) Washing the specimens with acetone and methanol.

3) Swabbing the test surface with acetone, washing in water, swabbing with concentrated nitric acid, washing in water, swabbing with distilled water, and finally swabbing with reagent grade methanol.

The atmosphere used for annealing was helium passed through an anhydrous $CaSO_4$ drying tower and activated charcoal held at $-196^{\circ}C$, or high purity argon passed through an anhydrous $CaSO_4$ drying tower. The two atmospheres worked equally well. For unknown reasons, pitting of the test surface would occasionally occur with either atmosphere.

III. EXPERIMENTAL TECHNIQUES

Dislocations were produced near the test surface by scratching or by damaging with a focused laser pulse. Berg-Barrett X-ray micrographs were taken to determine the "before test" position of the dislocations produced by the scratching or laser damage. The specimens were then tested using a torsion loading machine at various temperatures and stresses. After the test, another set of Berg-Barrett X-ray micrographs were taken to determine the final position of the dislocations.

Three or more tests were run at temperatures of 70°C, 23°C, -100°C and -150°C. The maximum shear stress at the outer edge of the specimens varied from 0.43 to 2.16×10^7 dynes/cm^2.

The experimental techniques used are described in detail in the sections which follow.

Methods for Producing Dislocations near the Test Surface

Dislocations of edge type and mixed type were produced on (111) planes close to the test surface by scratching in the $[11\bar{2}]$ and $[1\bar{1}0]$ directions respectively. The scratching was done using an Al_2O_3 whisker mounted on an arm attached to a calibrated torsion wire. Loads of 50 to 200 mg were used, and various speeds of scratching. A load of 50 mg and a scratching speed of 9 cm/minute were found to produce the best dislocations, i.e. with long lengths parallel to the scratch.

An enlargement of a typical Berg-Barrett X-ray micrograph showing the damage caused by scratches is given in Figure 4a. The enlargement in Figure 4a is not sufficient to show individual dislocations. Scratches in both the $[11\bar{2}]$ and $[1\bar{1}0]$ directions shown in Figure 4a produced dislocations parallel to the scratches. Both edge type and mixed dislocations were produced by scratches in the $[11\bar{2}]$ direction, with Burgers vector $\bar{b}_1$ for the edge and $\bar{b}_2$ or $\bar{b}_3$ for mixed dislocations, where $\bar{b}_1$, $\bar{b}_2$ and $\bar{b}_3$ are defined as shown on Figure 4a. Mixed dislocations with Burgers vector $\bar{b}_2$ or $\bar{b}_3$ were produced by scratches in the $[1\bar{1}0]$ direction.

Laser pulses were also used to produce dislocations. The arrangement used is shown in Figure 5. A pulse of energy from the ruby laser was focused to a 3 mm long line on the specimen surface by means of the cylindrical lens. The width of the line was kept to about 0.02 mm by the slits. The pulse duration was about 20 to 50 X 10^{-9} seconds and the energy of each pulse was about 0.08 joules. The neutral density filter and slits reduced the power incident on the specimen surface to about 0.01 joules; the energy actually absorbed by the specimen was not measured. Three or more pulses, spaced at ten minute intervals, were used at each damage location on the specimen.

The gas laser shown in Figure 5, which was operated at too low a power to damage the specimen, was aligned with the optic axis of the ruby laser and was used to orient the slits and specimen. The ruby

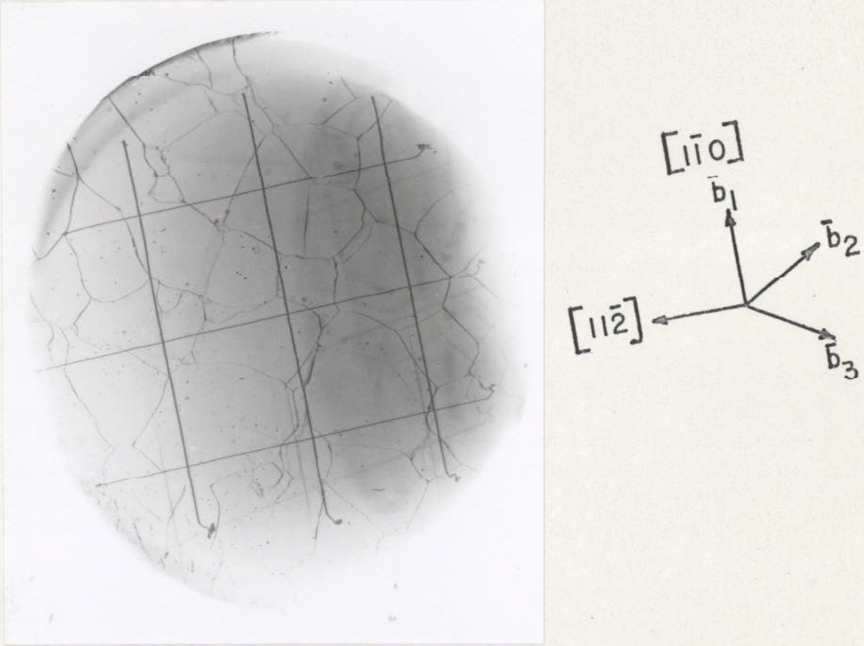

a. ENLARGEMENT OF BERG-BARRETT MICROGRAPH SHOWING SCRATCHING DAMAGE, ABOUT 5X

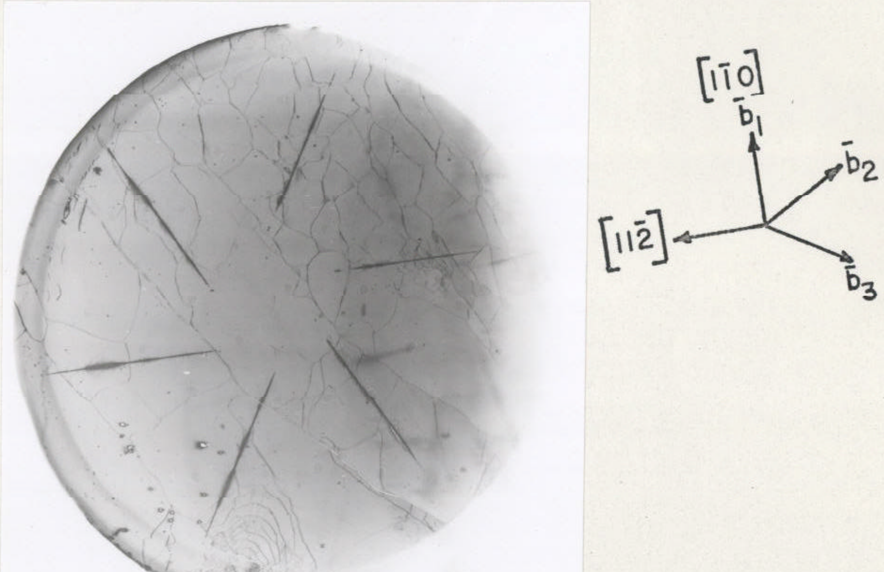

b. ENLARGEMENT OF BERG-BARRETT MICROGRAPH SHOWING LASER DAMAGE, ABOUT 5X

Fig. 4. Micrographs of Scratching and Laser Damage.

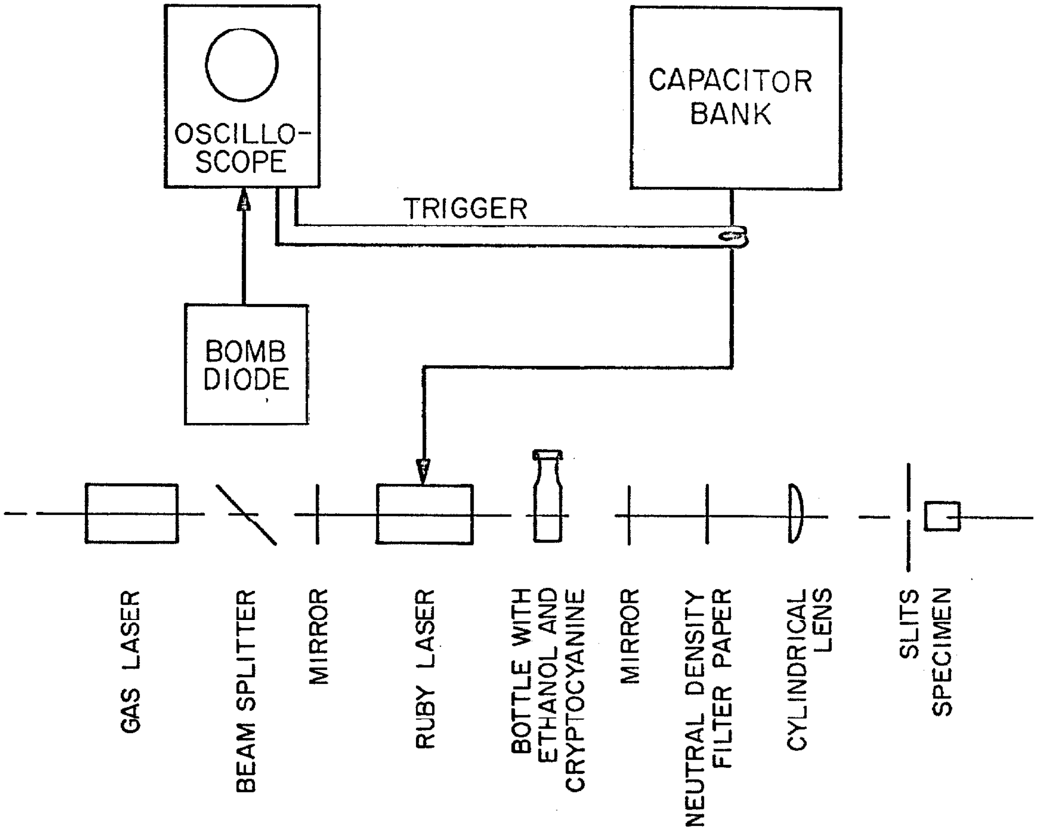

Fig. 5. Schematic of Laser Damaging Apparatus.

laser was made to discharge in a "giant" single pulse by adjusting the concentration of the cryptocyanine in ethanol solution. The bomb diode and oscilloscope were used to monitor the pulse. The mirrors established the optical cavity for the ruby laser.

An enlargement of a Berg-Barrett X-ray micrograph showing typical laser damage is shown in Figure 4b. The enlargement of Figure 4b is not sufficient to show individual dislocations. All of the laser damage lines are in $\langle 11\bar{2} \rangle$ type directions, and produce dislocations of mainly edge character nearly parallel to the damage line with Burgers vectors perpendicular to the damage line. All the damage lines are oriented approximately radially.

X-ray Technique for Observing Dislocations

Dislocations on (111) planes near the test surface of the specimen identified in Figure 1 were observed using the Berg-Barrett X-ray technique described by Turner, Vreeland and Pope (21). This technique makes use of the fact that the diffracted X-ray beam intensity in a Bragg reflection from a nearly perfect crystal is stronger in regions where strains such as those caused by dislocations distort the crystal lattice. As shown in Figure 6, X-rays from the target of the X-ray tube are collimated by slits and diffracted by the specimen on to the photographic plate. Because of the large size of the specimen compared to the X-ray source, only a portion of the specimen would diffract at a single angle between the X-ray beam and the specimen

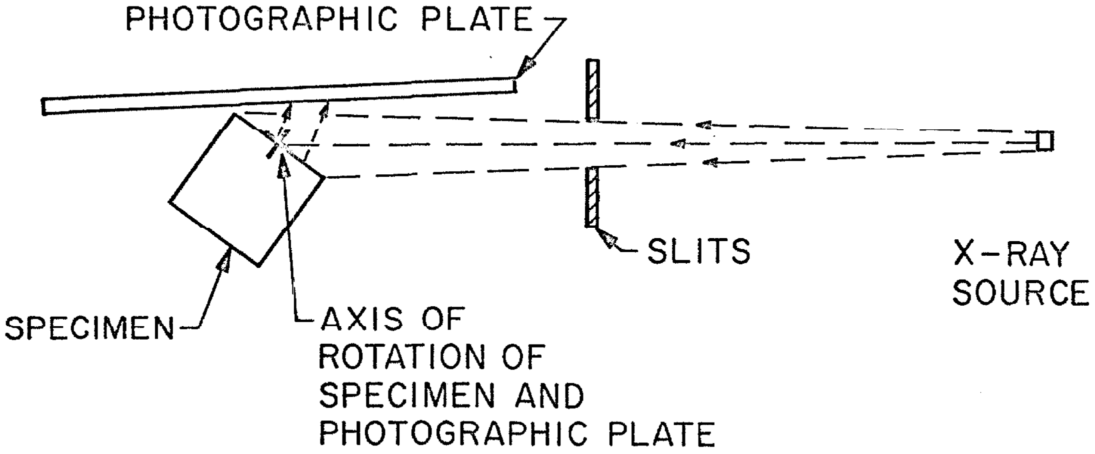

Fig. 6. Arrangement for Taking Berg-Barrett X-ray Micrographs.

surface. Therefore, the specimen and photographic plate were rotated as a unit about the axis shown in Figure 6 to cause the whole surface to diffract. The angle of rotation was varied through about 1/2 degree with a period of about four minutes. The photographic plate is placed nearly parallel to the X-ray beam, producing an unmagnified and slightly distorted image of the test surface. Figures 4a and 4b are enlargements of typical photographic images.

Characteristic iron radiation from a Machlett A-2 diffraction tube operating at 50KV and 7.5 ma was used. The focal spot was 1 mm square, the X-ray source to specimen distance was 16 cm, and the specimen to photographic plate distance ranged from 0.5 to 2 mm. The reflecting planes used were the $\{220\}$ planes in the test specimen as shown in Figure 7. The X-rays entered at an angle of eight degrees from the plane formed by the $[111]$ axis and the normal to the reflecting plane, as shown on Figure 7a. This location for the X-ray beam was chosen to avoid reflections from other crystallographic planes. The X-rays approached the test surface at an angle of 8°, as shown on Figure 7b. Kodak high resolution plates were used, and no filter was used except for a 0.012 cm thick black plastic film to exclude light. The resolution obtained by this technique was about 10μ.

The Burgers vector of a dislocation can be determined using the fact that a dislocation will not alter the intensity of the diffracted X-ray beam, and therefore, will not be imaged on the photographic

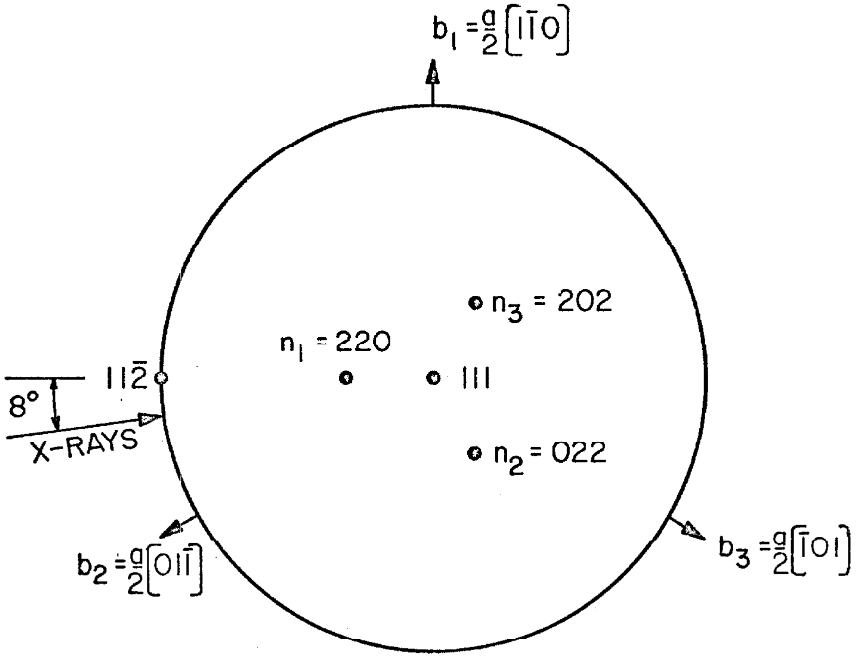

a. (111) STEREOGRAPHIC PROJECTION SHOWING DIRECTIONS OF BURGERS VECTORS AND REFLECTING PLANES. NOTE THAT $\bar{b}_i \cdot \bar{n}_j = 0$ FOR $i = j$, $\bar{b}_i \cdot \bar{n}_j \neq 0$ FOR $i \neq j$. X-RAYS FOR REFLECTION FROM THE n_1 PLANES ARE ALSO SHOWN.

Fig. 7. Crystallographic Orientation of Reflecting Planes and Dislocation Burgers Vectors.

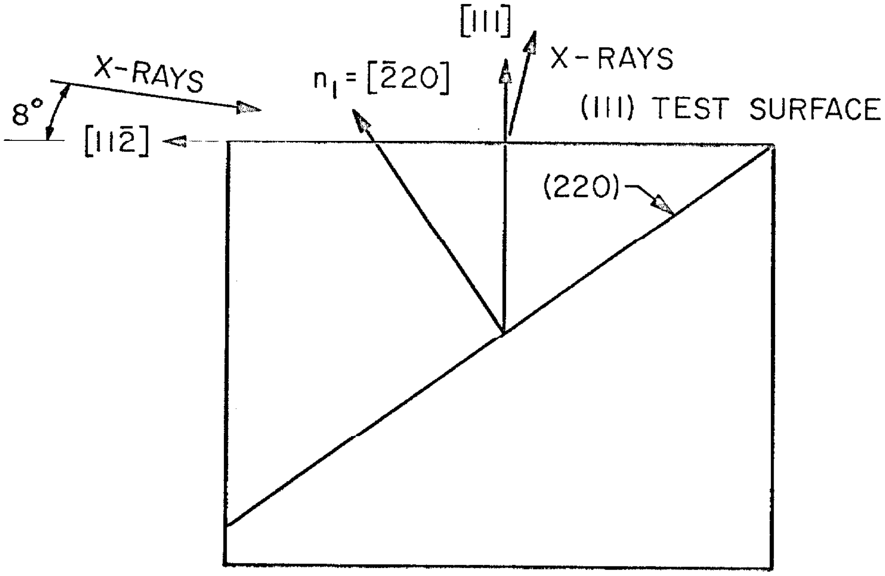

b. SECTION THROUGH TEST SPECIMEN SHOWING (220) REFLECTING PLANE AND (111) SURFACE. X-RAYS FOR THE (220) REFLECTION ENTER AND LEAVE AS SHOWN, EXCEPT THEY ARE ROTATED OUT OF THE PLANE SHOWN BY EIGHT DEGREES.

Fig. 7. continued

plate, if $\bar{b}\cdot\bar{n} = 0$ where $\bar{b}$ is the Burgers vector and $\bar{n}$ is the normal to the reflecting plane. As shown in Figure 7a, for each of the three possible Burgers vectors there is one and only one {220} type reflecting plane for which a dislocation with that Burgers vector will not be imaged. By taking micrographs using all three reflecting planes, it is, therefore, possible to determine the Burgers vectors of all the dislocations.

Loading System

The torsion machine described by Pope, Vreeland and Wood (22) was used to produce torsion stress pulses of 15 to 108 μsec duration. The maximum stress produced at the outer edge of the specimen varied from 0.43 to $2.16\text{X}10^7$ dynes/cm^2. The torsion machine operates by producing a zero mode torsional stress wave which propagates down a cylindrical rod and through the specimen, and is then reflected from a free end and propagates up the rod and through the specimen as an unloading wave.

The specimen loading procedure was as follows: The test surface of the specimen was glued to a polycrystalline aluminum gage bar of the same diameter as the specimen as shown in Figure 8. The polycrystalline gage bar was permanently attached to the torsion machine which was constructed of titanium. A rod of polycrystalline aluminum was then glued to the bottom of the test specimen; this rod is identified as the extender in Figure 8. A step input of torsional

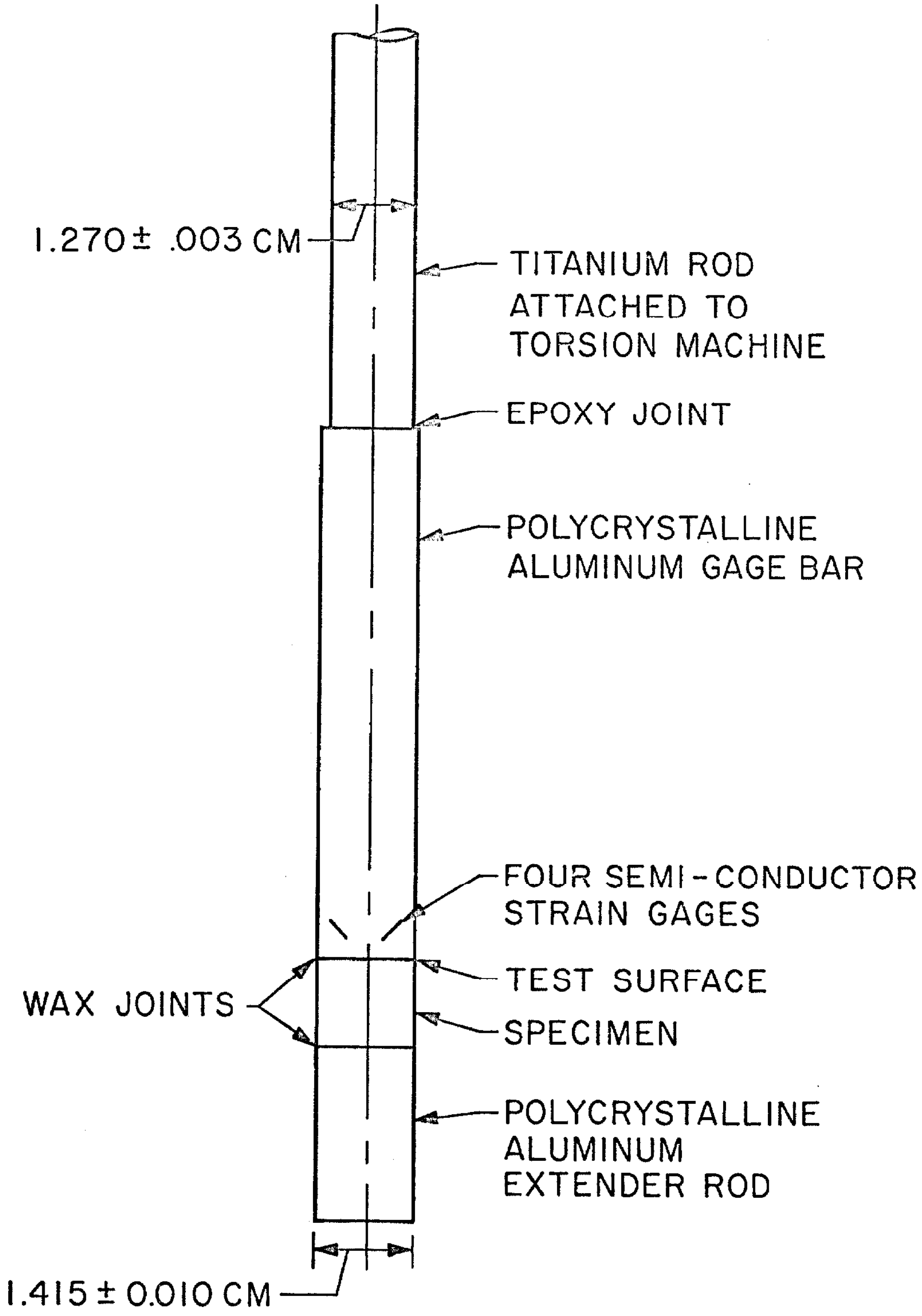

Fig. 8. Specimen and Extender Glued to Torsion Machine for Room Temperature Test.

stress was produced by the torsion machine and propagated down the titanium rod of the torsion machine at a speed $(G/\rho)^{1/2}$ where G is the modulus of rigidity and ρ is the mass density of the rod. The stress wave propagated through the gage bar, the specimen, and the lower extender rod, and reflected from the free end of the extender as an unloading wave of the same magnitude as the original loading wave. The stress duration at the test surface of the specimen was thus the time taken for the loading wave to propagate through the specimen and extender plus the time taken for the unloading wave to propagate back to the test surface. The different durations of the stress pulses in different tests were obtained by varying the length of the specimen plus lower extender rod.

In the polycrystalline rods the stress wave has an elastic stress distribution such that the shear stress τ is linearly proportional to the radius:

$$\tau = \frac{Tr}{J} \qquad [2]$$

where T is the torque, r the distance from the specimen axis, and J is the polar moment of the cross-section. The single crystal specimen behaves approximately in an isotropic manner, as is shown in Appendix A, and the stress distribution on the (111) test surface slip planes is approximately that given in equation [2].

The magnitude of the stress pulse was determined by measuring the strain on the surface of the gage bar using 500 ohm semiconductor strain gages attached to the gage bar. The gage output was monitored using an oscilloscope as described in reference (22). A typical stress pulse is shown in Figure 9.

The torsion machine uses a 1.27 cm diameter titanium rod. The diameter of the aluminum gage bar was selected to prevent stress wave reflections at the titanium to aluminum interface. As shown in reference (10), a torsional wave will not be reflected at the interface of two cylindrical bars of different radii if the wavelengths are long compared to the radius change and if the quantity

$$z = a^4 (G\rho)^{1/2} \qquad [3]$$

is continuous across the interface, where z is the torsional acoustic impedance, G is the modulus of rigidity, ρ is the mass density, and a is the radius. The test specimen radius was made the same as the gage bar radius since the acoustic properties of a [111] oriented aluminum crystal are not very different from polycrystalline aluminum.

Techniques for Gluing Specimens to Gage Bar

The gluing technique used at each temperature had to satisfy three basic requirements:

1. The gluing technique should not damage the test surface or cause any motion of the dislocations. This required the shear stresses on the test surface due to the glue to be less than 0.3×10^6 dynes/cm^2.

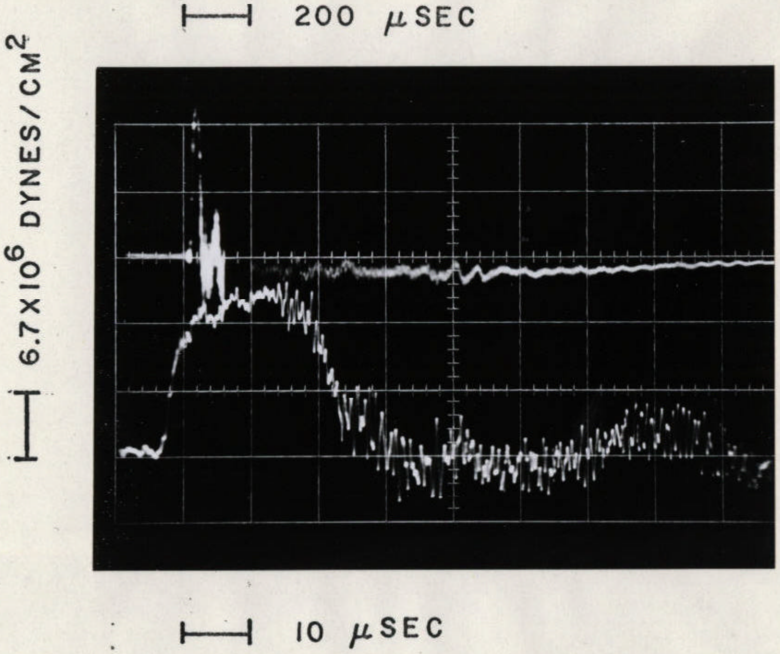

Fig. 9. Typical Torsion Stress Pulse Record.

2. The glue had to have a high enough modulus of rigidity and the glue joint had to be thin enough so that the stress wave could be transmitted without reflection or excessive decrease in its rise time. Appendix B contains an analysis of the problem of transmitting a torsion wave in a cylindrical rod across a gap containing a low modulus material.
3. The glue should not fail when subjected to a maximum shear stress of about $2X10^7$ dynes/cm^2 applied for times up to 100 μsec.

Several different glues for each temperature were tried. Many glues had to be rejected because differential thermal expansion between the glue and the specimen damaged the specimen test surface. A glue was tested for suitability by going through the entire gluing and ungluing procedure described below, but without passing a torsion pulse through the specimen. The specimen was then examined by taking Berg-Barrett X-ray micrographs to determine if any damage or dislocation motion had occurred. The gluing techniques described below were found to produce no dislocation motion or surface damage.

The glue used for room temperature tests was Quartz Type Sticky Wax with a melting temperature of 75°C, supplied by the Corning Rubber Company, Brooklyn, New York. The extender, which is identified in Figure 8, was first heated to just above the melting point of the wax, and the wax was applied to the surface to be bonded to the specimen.

The bottom of the specimen, which was at room temperature, was then pressed on to the extender. The gage bar was then heated to just above the melting point of the wax; the wax was then applied, and the specimen and extender, which were at room temperature, were gently pressed on to the gage bar. Subsequent to testing, the extender was removed by heating it sufficiently to allow it to slide off, and the specimen was removed by heating the gage bar until the specimen slid off. The specimen was then washed in xylene to remove the remaining wax.

Low temperature tests were performed using mixtures of glycerin and ethanol as glues. Three parts glycerin to two parts ethanol was used at -100°C, and one part glycerin to five parts ethanol was used at -150°C. The procedure used for low temperature tests was the following:

1. The specimen and extender were assembled in position below the gage bar as shown in Figure 10 at room temperature, with the appropriate glycerin-ethanol mixture already in the gaps between the specimen and extender and specimen and gage bar. The extender was supported on a teflon ball seat which rested on a movable yoke. The alignment of the specimen to the gage bar and to the extender was maintained by thin bakelite alignment collars as shown in Figure 10.
2. The gage bar, specimen, and extender were then cooled down

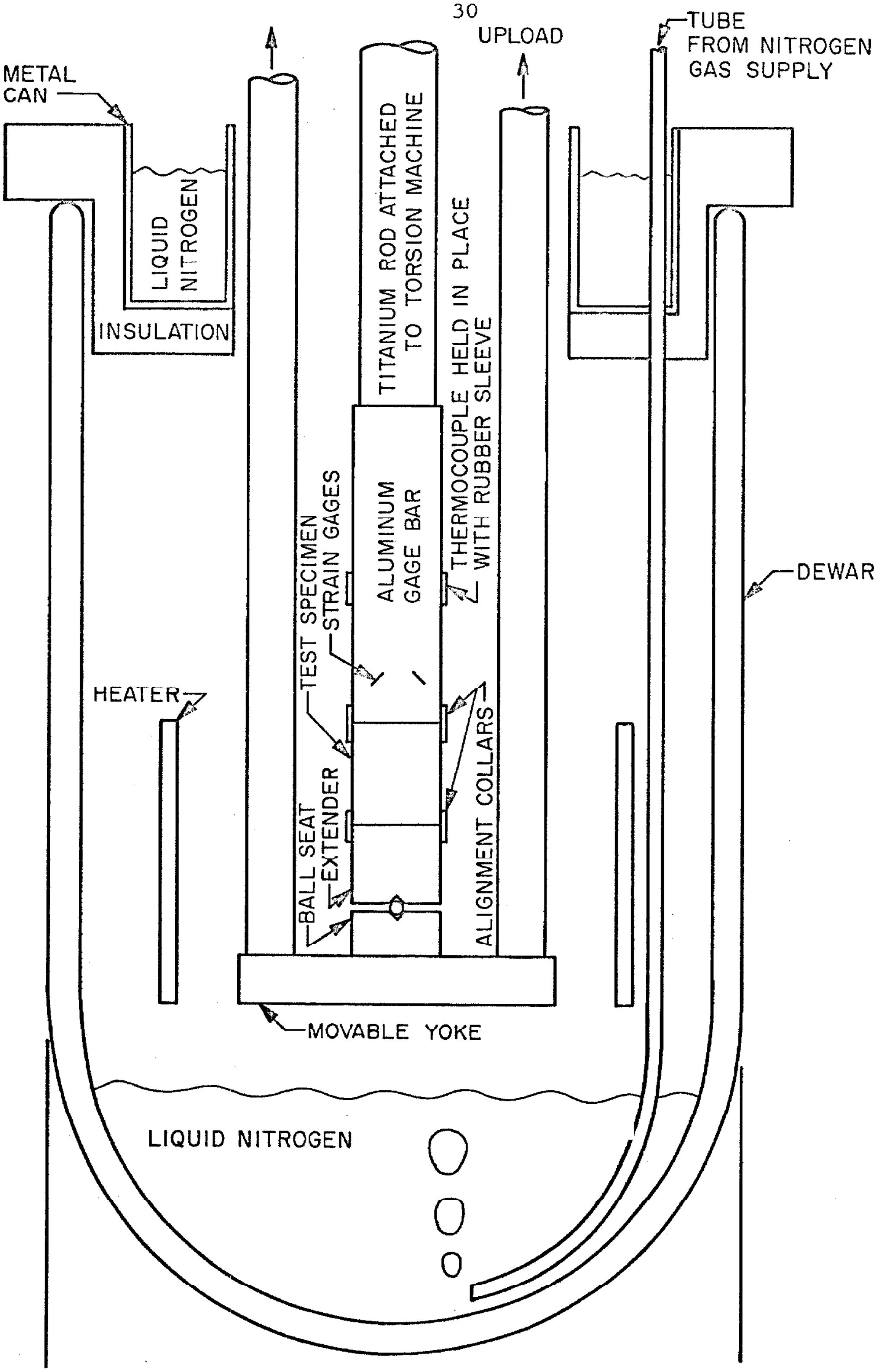

Fig. 10. Arrangement for Low Temperature Tests.

to the test temperature in the apparatus shown in Figure 10. The cooldown rate was about 5°C/min. The cooldown, and subsequent temperature stabilization and heatup, were controlled by varying the rate at which dry nitrogen gas was bubbled into the liquid nitrogen bath and by varying the voltage supplied to the heater shown in Figure 10.

3. The gaps filled with the glycerin-ethanol mixtures were closed by applying a compressive load of three pounds with the movable yoke shown in Figure 10. The load was applied during the cooldown at -90°C for the -100°C tests and at -110°C for the -150°C tests.
4. The temperature was stabilized at the test temperature and maintained for ten minutes for -100°C tests and for five minutes for -150°C tests. The compressive load was then removed and the torsion test performed.
5. The assembly was heated up at 5°C/min. to room temperature. As the glycerin-ethanol mixture softened, the gaps opened and the specimen and extender settled down on to the ball seat, but were held in place by the alignment collars.

The glue used for the 70°C tests was a 120°C melting temperature wax supplied by Fiber-Resin Corporation, Burbank, California which was filled with levigated alumina powder until the wax-powder mixture would just flow when above 120°C. The 70°C test procedure was as follows:

1. The specimen and extender were assembled in position at room temperature as shown in Figure 11. Chips of the wax-alumina powder mixture were placed in the extender to specimen and specimen to gage bar gaps. The extender rested on a ball seat which was supported by a movable yoke. The specimen and extender alignment was maintained by the use of thin bakelite alignment collars. A thin rubber sleeve protected the extender, specimen, and gage bar from the glycerin bath.
2. The glycerin bath was heated to 125°C to melt the wax in the gaps. A compressive load of three pounds was applied with the movable yoke shown in Figure 11 to close the gaps and the temperature was maintained at 125°C for ten minutes with the load applied.
3. The glycerin was allowed to cool to 70°C. After the temperature was stabilized at 70°C for five minutes the compressive load was removed and the test performed.
4. After testing, the gage bar, specimen and extender assembly was removed from the torsion machine and transferred to a 70°C bath of an aromatic hydrocarbon solvent. The solvent was then heated until the wax-alumina powder joints softened and the extender and specimen could be removed without damaging the specimen.

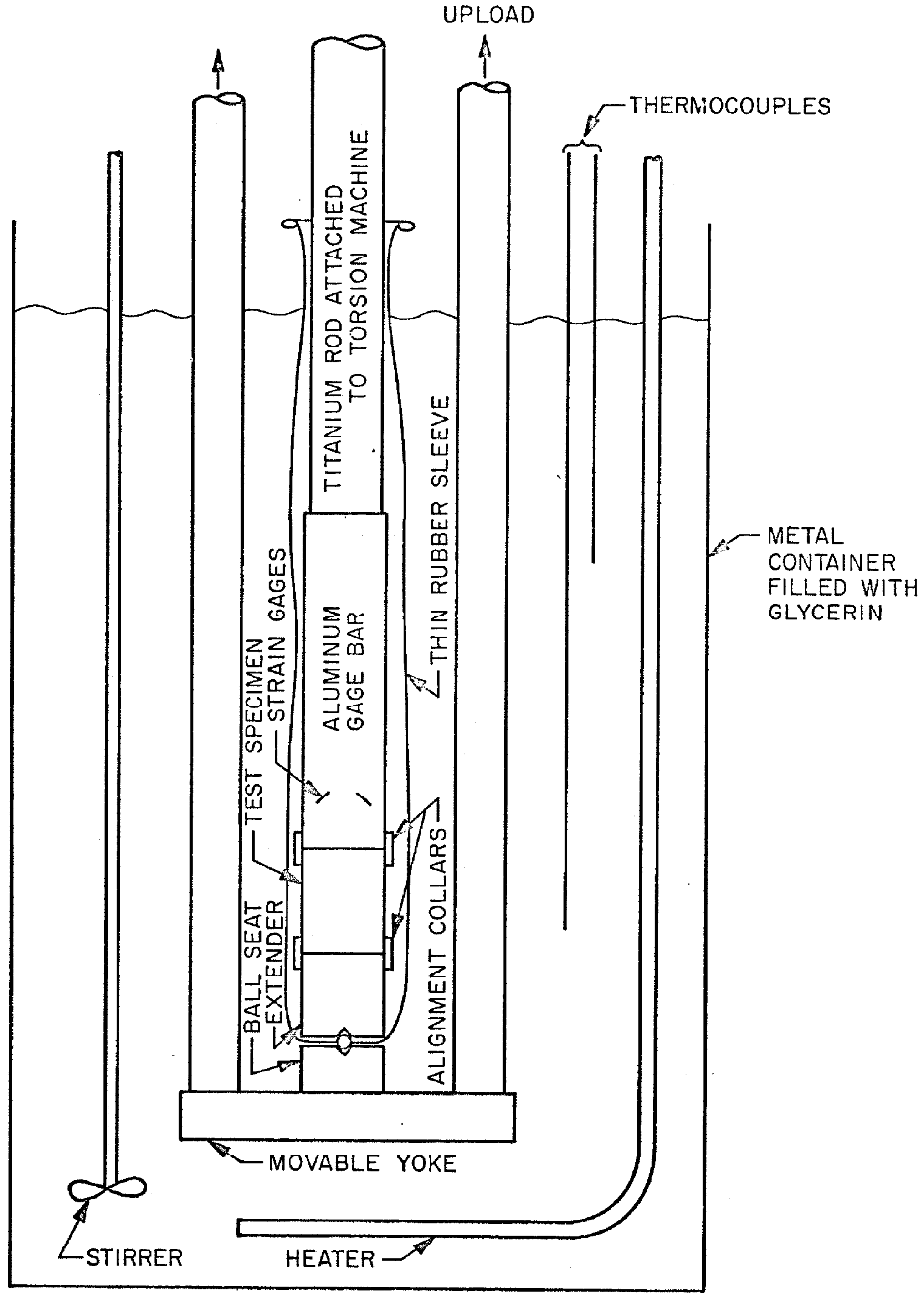

Fig. 11. Arrangement for 70°C Tests.

Temperature Measurement

Temperature measurement for low temperature tests was by copper-constantan thermocouples attached to the gage bar and shielded from the atmosphere with a rubber sleeve as shown in Figure 10. Trial runs demonstrated that the gage bar and specimen temperature agreed within 2°C; the overall accuracy of the temperature measurement is estimated to be ± 5°C.

Temperature measurement for the 70°C tests was by copper-constantan thermocouples in the glycerin bath shown in Figure 11. Trial runs showed that the glycerin and specimen temperatures agreed within 2°C; the overall accuracy of the temperature control is estimated at ± 5°C.

The specimen temperature was not measured during room temperature tests. However, adequate time after gluing was allowed (1/2 hour or more) to permit the specimen to attain room temperature (23°C).

IV. EXPERIMENTAL RESULTS

Dislocation Displacement Measurements

Figure 12 contains enlargements of Berg-Barrett X-ray micrographs showing dislocation positions before and after torsion testing for a scratched specimen and for a laser damaged specimen. The maximum displacement of dislocations during the test was measured on the Berg-Barrett X-ray micrographs using a microscope fitted with a calibrated filar eye piece. Each location along a scratch or line of laser damage where dislocation displacement reached a maximum provided a data point. The measurements were not made where the dislocations appeared to have been impeded by subgrains or where the "after test" dislocations were tangled, i.e. where the leading dislocation was not free of entanglement for a length of 0.1 mm or more. Therefore, the dislocation velocities calculated from these measurements are the maximum values for all dislocations which were observed to move at a given temperature and stress.

The displacements measured from the micrographs were used directly in calculating the dislocation velocity since the maximum error in distances on the micrographs relative to actual distances in the crystal was calculated to be less than five percent.

It can be seen from Figure 12 that the dislocations moved out from only one side of the scratch or laser damage. This occurs since the scratching or laser damage should produce dislocations of the same

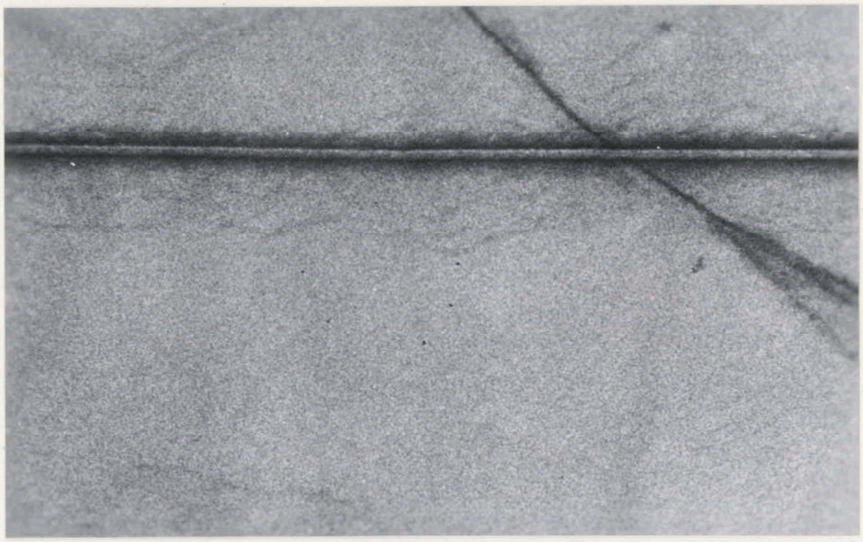

BEFORE TEST

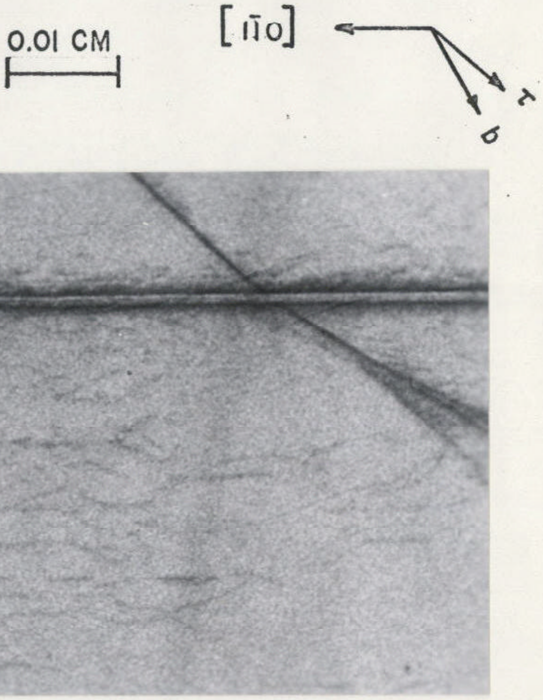

AFTER TEST

a. SCRATCHED SPECIMEN

Fig. 12. Berg-Barrett X-ray Micrographs Showing Dislocations Before and After Torsion Tests.

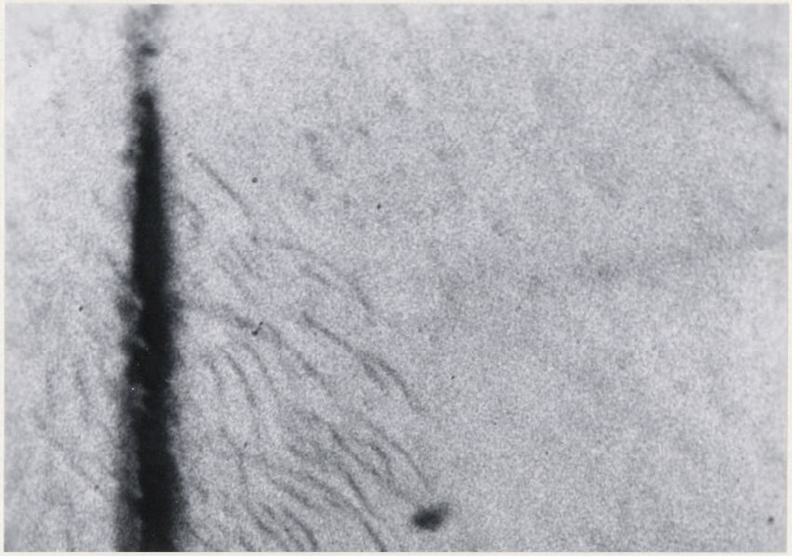

BEFORE TEST

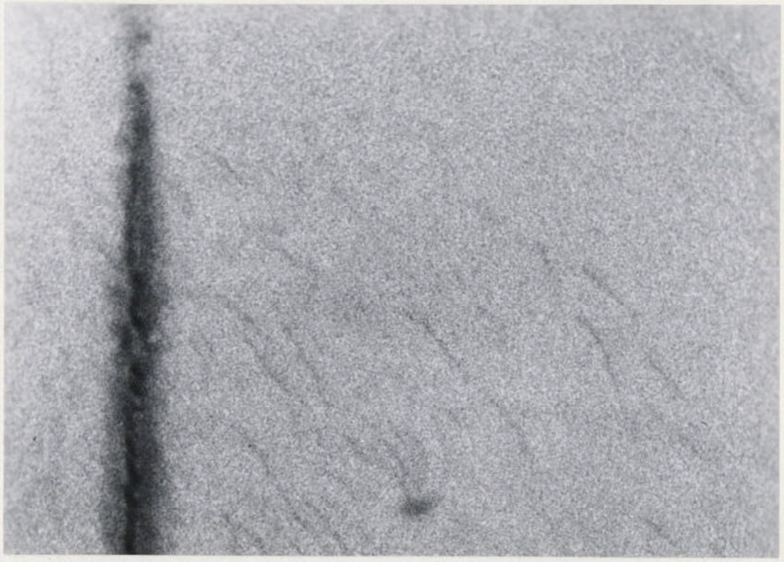

AFTER TEST

b. LASER DAMAGED SPECIMEN

Fig. 12. Continued

sign on both sides, as shown in Figure 13. The forces due to scratching or laser induced thermal expansion tend to produce dislocations with extra planes on the surface side of the dislocation slip plane. The applied shear stress during the torsion test tends to return the dislocations on one side to the scratch or laser damage while it tends to move those on the other side away from the scratch or laser damage. There were occasional instances of dislocations moving in both directions, showing that some dislocations of the opposite sign were produced.

The dislocation displacements observed in a typical test are plotted in Figure 14 as a function of the product of the radius, R, and the stress resolution factor, cos θ, where θ is the angle between the tangential direction and the Burgers vector. The approximately linear trend of the data in Figure 14 shows that the dislocation velocity is approximately linearly proportional to the resolved shear stress, as discussed in detail in Appendix C.

Stress and Time Measurements

Figure 9 is a typical torsion stress pulse record. The top trace shows the long-time behavior of the stress, and the lower trace shows the stress pulse itself in greater detail. The method used to obtain the average stress and appropriate pulse duration from the record was as follows:

1. Stress pulses were measured using strain gages located about 0.7 cm from the end of the gage bar. As shown in Figure 15a, a stress pulse with the gage bar alone, without a specimen or

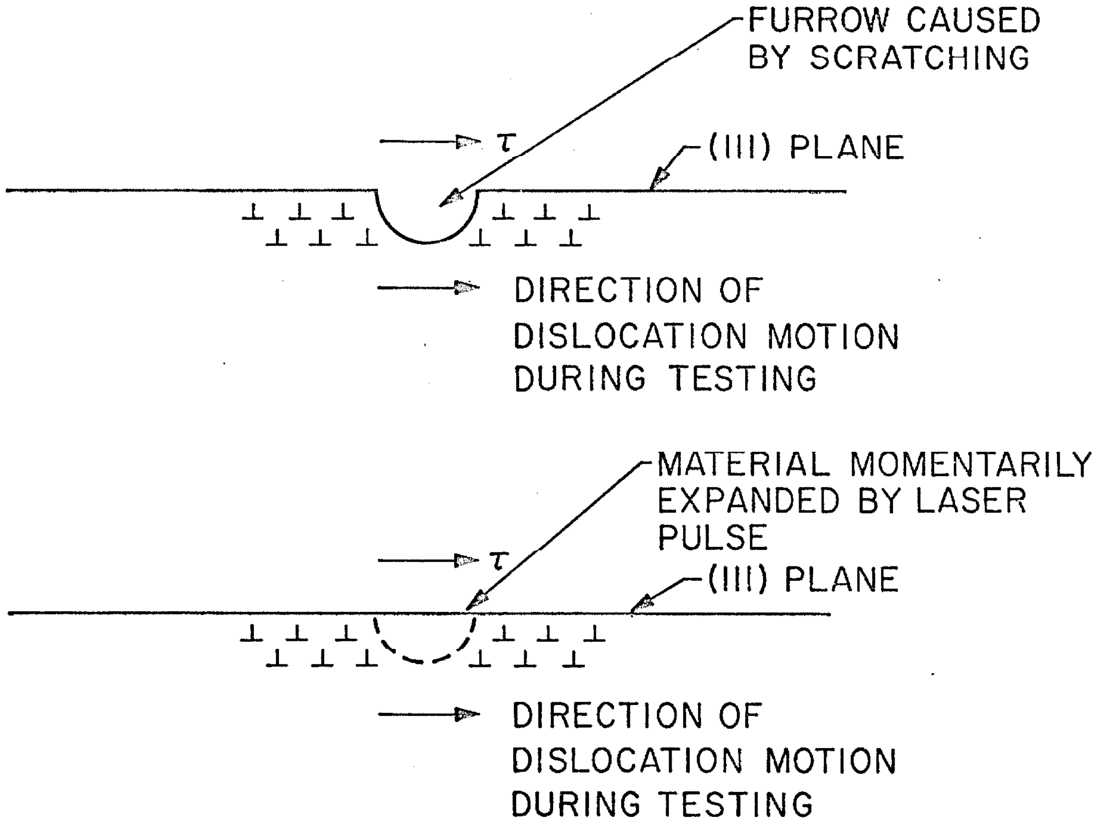

Fig. 13. Dislocation Configuration Caused by Scratching and Laser Damage.

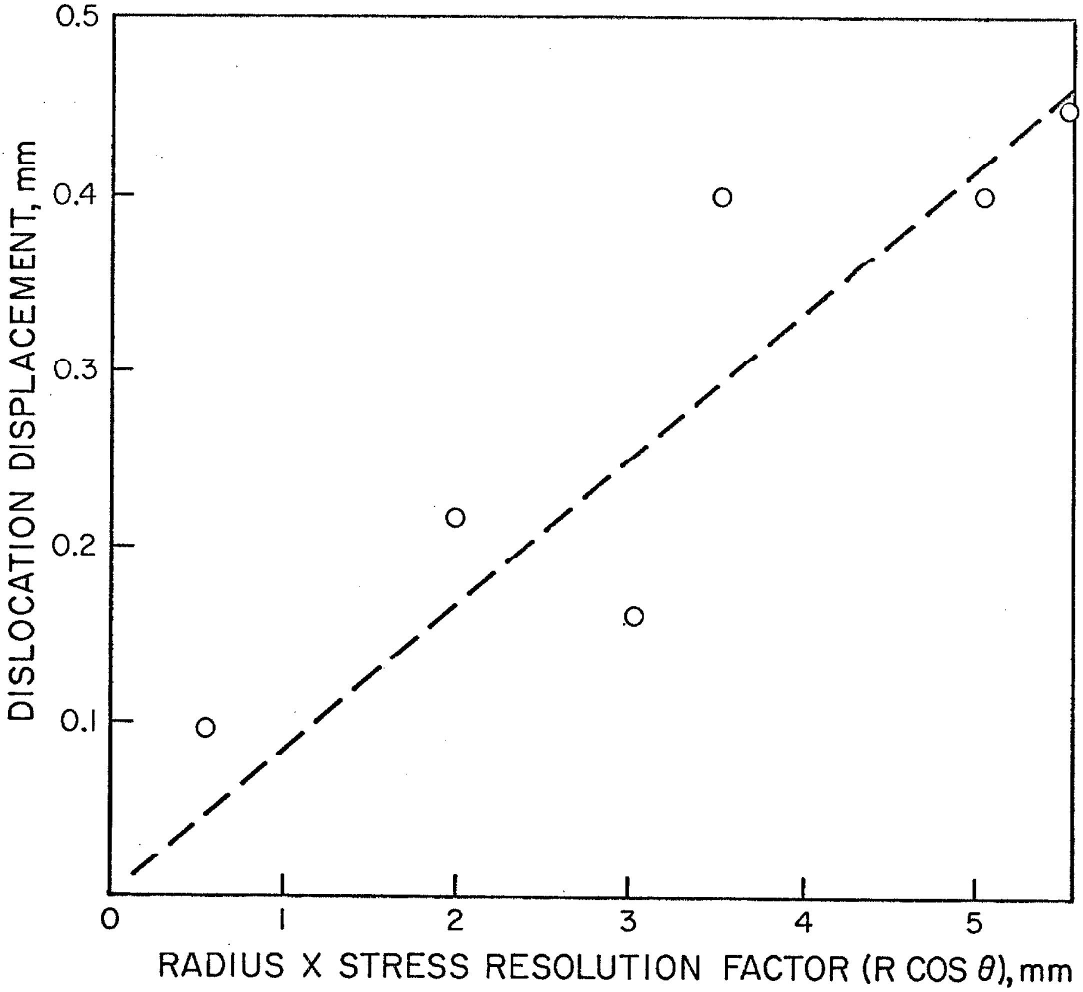

Fig. 14. Dislocation Displacement vs Product of Radius and Stress Resolution Factor (Rcosθ) for Test 17.

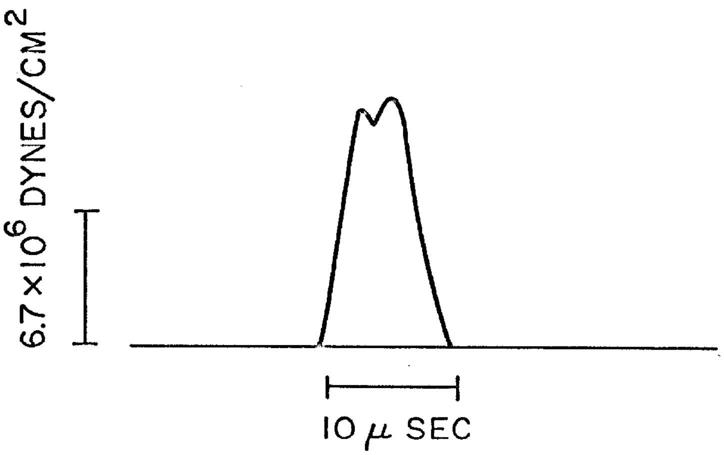

a. RECORD OF TORSION STRESS PULSE WITH GAGE BAR ALONE.

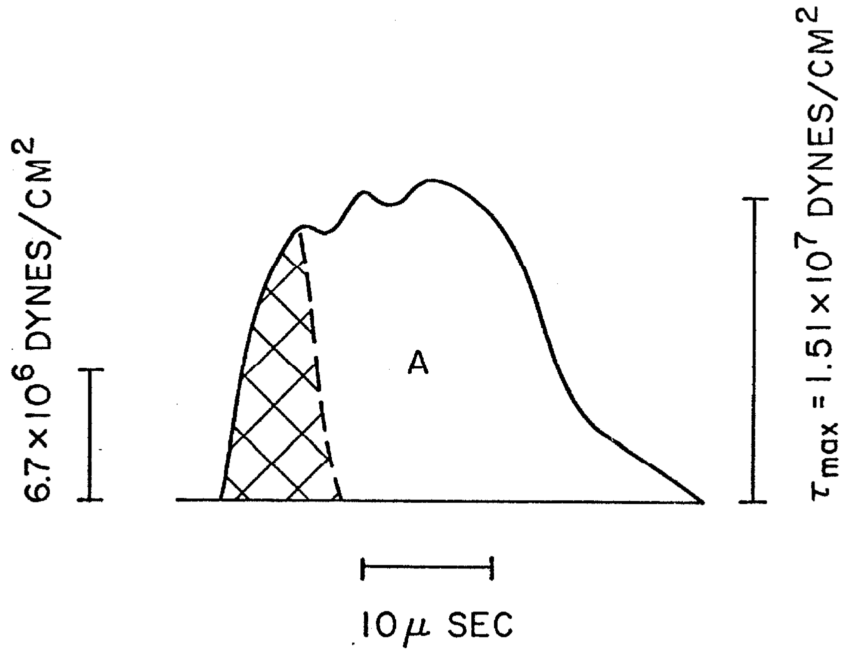

b. RECORD OF TORSION STRESS PULSE (FROM FIGURE 9) WITH SPECIMEN AND EXTENDER. CROSS-HATCHED AREA DUE TO GAGE BAR ALONE.

Fig. 15. Torsion Stress Pulse Records.

lower extender rod attached, had a short duration corresponding to the time taken for the stress wave to pass the gages, be reflected from the free end as an unloading wave, and to return to the gages. As shown in Figure 15b, the stress pulse duration was increased by attaching a specimen and extender to the gage bar. The additional area of the stress pulse, marked A in Figure 15b, is thus the portion of the stress pulse due to the stress wave travelling down and back through the specimen and extender, and gives the stress-time history at the test surface. This area, A, was measured with a planimeter.

2. The maximum stress τ_{max}, was taken from the pulse record; the short duration noise was averaged out in selecting this maximum stress. The numerical value of this maximum stress was obtained by comparison of the pulse record with records of previous tests run with dummy polycrystalline aluminum specimens and rigid glues.
3. The area A under the stress-time curve was considered to be equivalent to a square pulse with the same magnitude, τ_{max}, and an equivalent duration, t_o, obtained by dividing the area A by τ_{max}.
4. The stress and duration of the equivalent square pulse, τ_{max} and t_o, were then used in the calculation of the stress and

velocity of the dislocations.

The above procedure does not introduce any errors in the ratio of velocity to stress since the dislocation velocity is linearly proportional to stress, as was shown above. This conclusion is shown by:

$$D = \int_0^\infty v(t)dt = k\int_0^\infty \tau(t)dt \qquad [4]$$

$$\begin{aligned} D &= k \text{ (area under stress-time curve)} \\ &= k\ \tau_{max}\ t_o \qquad [5] \end{aligned}$$

$$v = D/t_o = k\ \tau_{max} \qquad [6]$$

where D is the displacement, $v(t)$ is the instantaneous velocity which equals $k\ \tau(t)$, $\tau(t)$ is the instantaneous maximum stress, k is a constant including factors such as the radius of the dislocation and the stress resolution factor, τ_{max} and t_o are the stress pulse amplitude and duration obtained as discussed above, and v is the calculated dislocation velocity. If the value of τ_{max} is incorrectly selected, the value of v changes proportionately and no error is introduced into the ratio of dislocation velocity to applied stress.

The values of τ_{max} and t_o for all the tests used in this experiment are listed in Table I.

Applied Resolved Shear Stress Determination

The applied stress acting on a dislocation was obtained by measuring the distance of the dislocation from the center of the

TABLE I

TEST	TEMPERATURE, °C	τ_{max}, 10^6 dynes/cm^2	t_o, μsec
16	-150	10.8	17.3
17	-150	15.1	18.2
18	-150	15.1	17.4
19	-150	12.9	24.9
10	-100	15.1	22.1
12	-100	21.6	15.3
13	-100	15.1	20.0
14	-100	21.6	18.0
15b	-100	15.1	23.5
4	23	21.6	21.7
6	23	4.3	108
15a	23	21.6	17.5
20	70	15.1	40.0
21	70	15.1	31.9
22	70	21.6	22.8

specimen, and assuming a linear stress distribution as given in equation [2] in the section on experimental techniques. A linear stress distribution is approximately correct for a [111] oriented aluminum specimen, if the stress remains elastic, as is shown in Appendix A. In addition, a linear stress distribution requires that there not be excessive plastic flow in the specimen. The amount of plastic flow which occurred during the tests listed in Table I did not significantly affect the stress distribution in regions where dislocation velocity was measured as is shown below.

Examination of the Berg-Barrett X-ray micrographs showed that in the central, low stress region of the specimens essentially no dislocation motion occurred except for the artificially introduced dislocations, i.e. there was negligible plastic flow in the central region. In some tests, dislocation multiplication and motion was evident in the outer regions of the specimen, i.e. plastic flow occurred. In the worst case, plastic flow occurred in the outer 20% of the radius. Using the conservative assumption of an elastic-perfectly plastic material, it is shown in Appendix D that the stress in the central elastic region is only increased 8% in this worst case.

The resolved shear stress acting on a dislocation was obtained by using the relation

$$\tau_r = \tau \cos\theta \qquad [7]$$

where τ_r is the resolved shear stress, τ is the applied shear stress, and θ is the angle between τ and the Burgers vector of the dislocation. The Burgers vector was determined from the Berg-Barrett X-ray micrographs as discussed in the experimental procedures section of this thesis, while the direction of τ was assumed to be perpendicular to the radial line passing through the dislocation.

Dislocation Velocities

Dislocation velocities were calculated by dividing the measured displacement by the torsion stress pulse duration. It was assumed that the dislocation velocity was in phase with the applied stress, i.e. that the dislocation acceleration time was negligible; this assumption is justified as is shown later in the discussion section. The dislocation velocity data are plotted as a function of resolved shear stress for each temperature in Figure 16. The data for each temperature are fitted by a straight line from the origin through a point obtained by averaging all the stress-velocity data for that temperature. This procedure was used since the data seem to roughly fit a linear stress distribution. The straight lines for each temperature are:

$$70^{\circ}\text{C:} \quad v = 0.985\text{X}10^{-4}\tau_r$$

$$23^{\circ}\text{C:} \quad v = 1.16\text{X}10^{-4}\tau_r$$

$$-100^{\circ}\text{C:} \quad v = 1.50\text{X}10^{-4}\tau_r$$

$$-150^{\circ}\text{C:} \quad v = 1.96\text{X}10^{-4}\tau_r$$

where v is the velocity in cm/sec and τ_r is the resolved shear stress in dynes/cm^2. Other curves could have been fitted to the data; however,

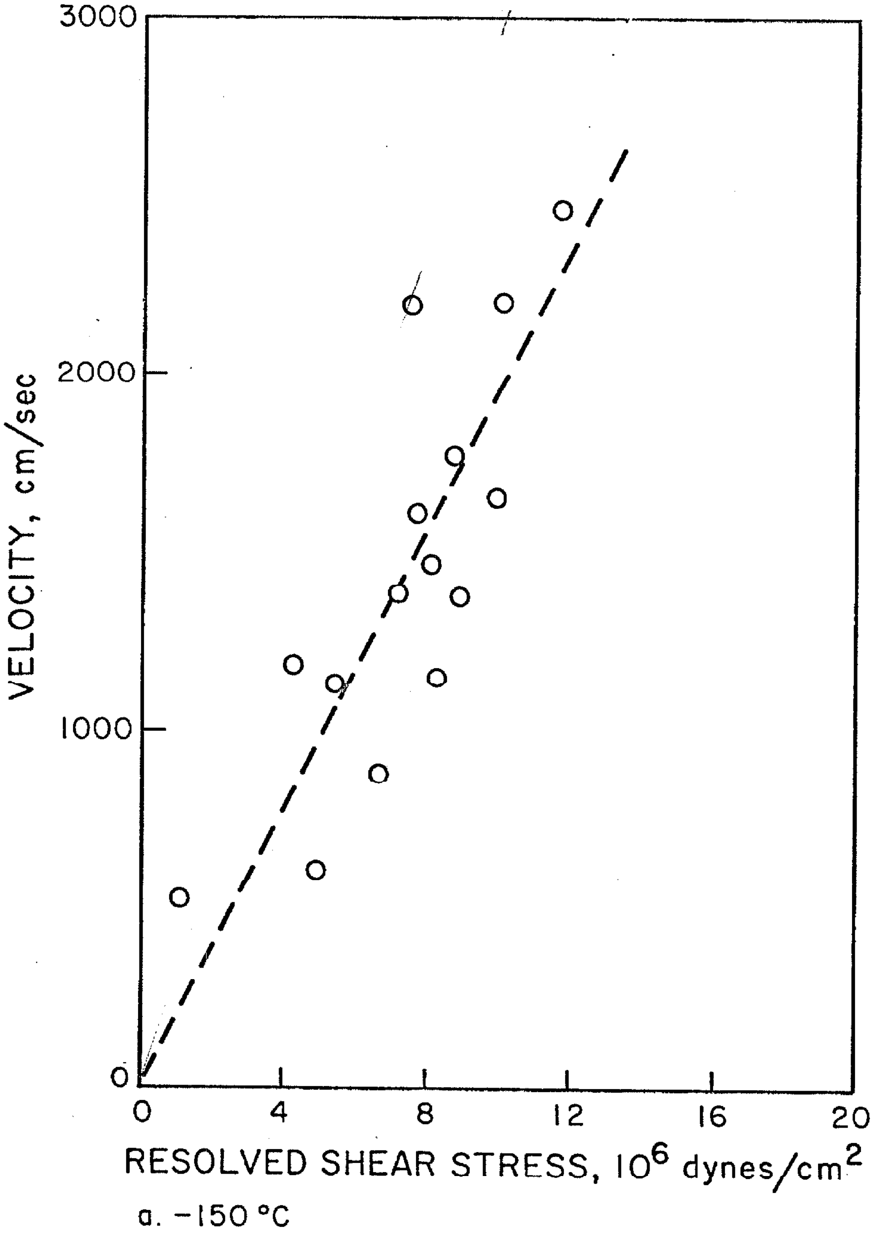

Fig. 16. Dislocation Velocity vs Resolved Shear Stress.

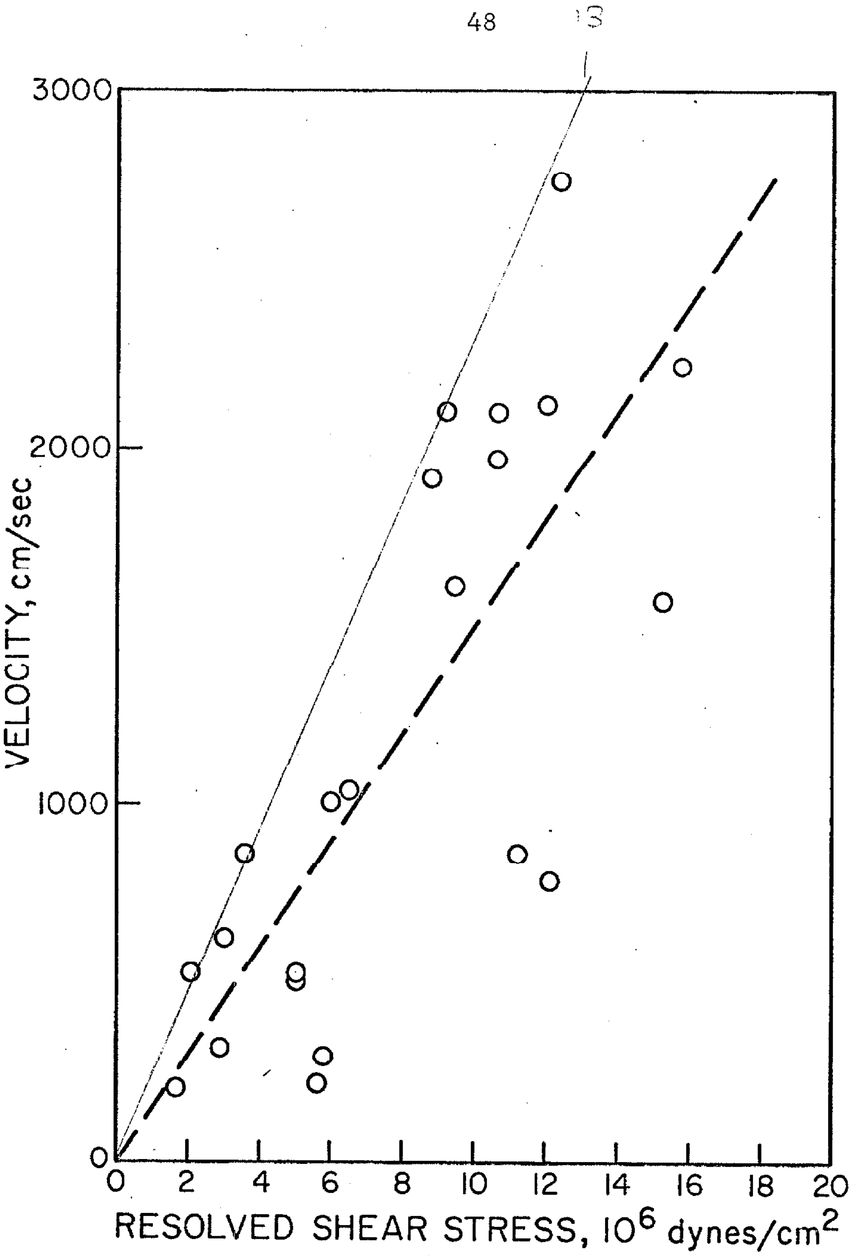

b. -100 °C

Fig. 16. Continued.

19

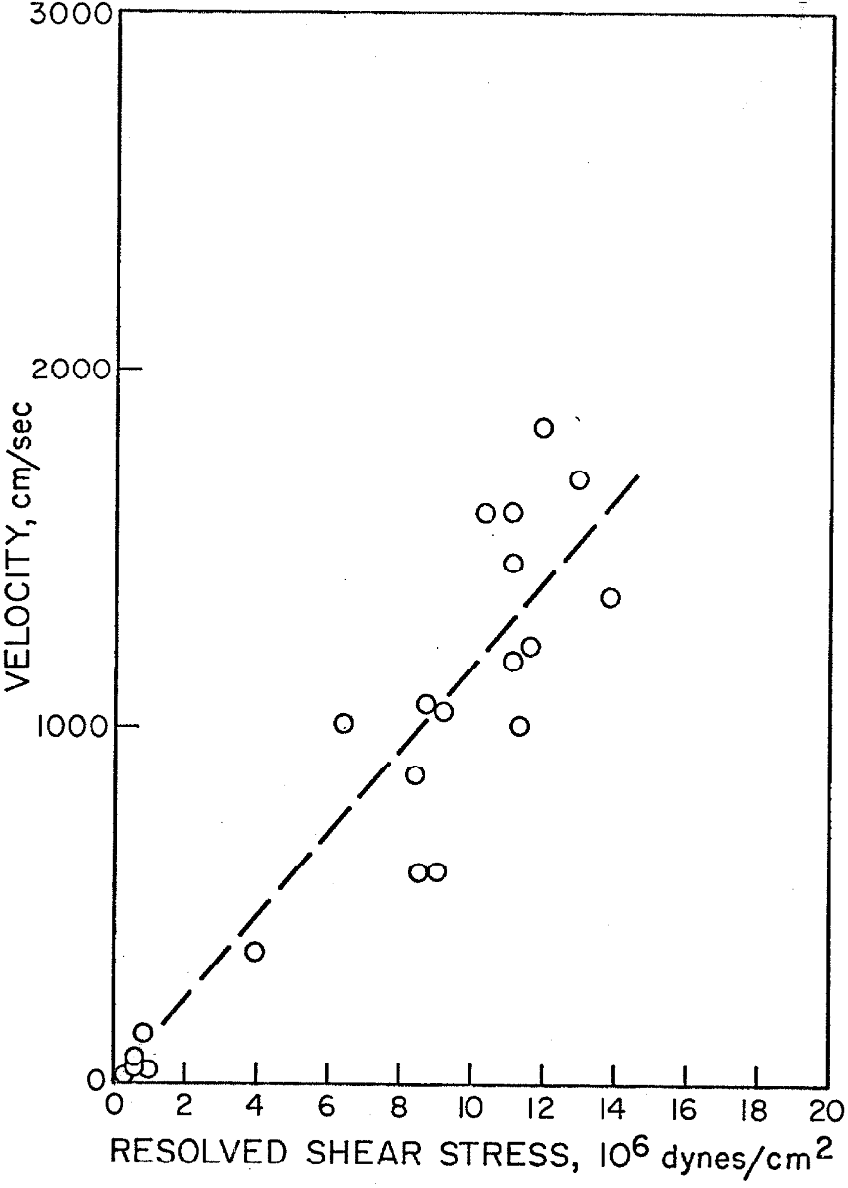

c. ROOM TEMPERATURE (23°C)

Fig. 16. Continued.

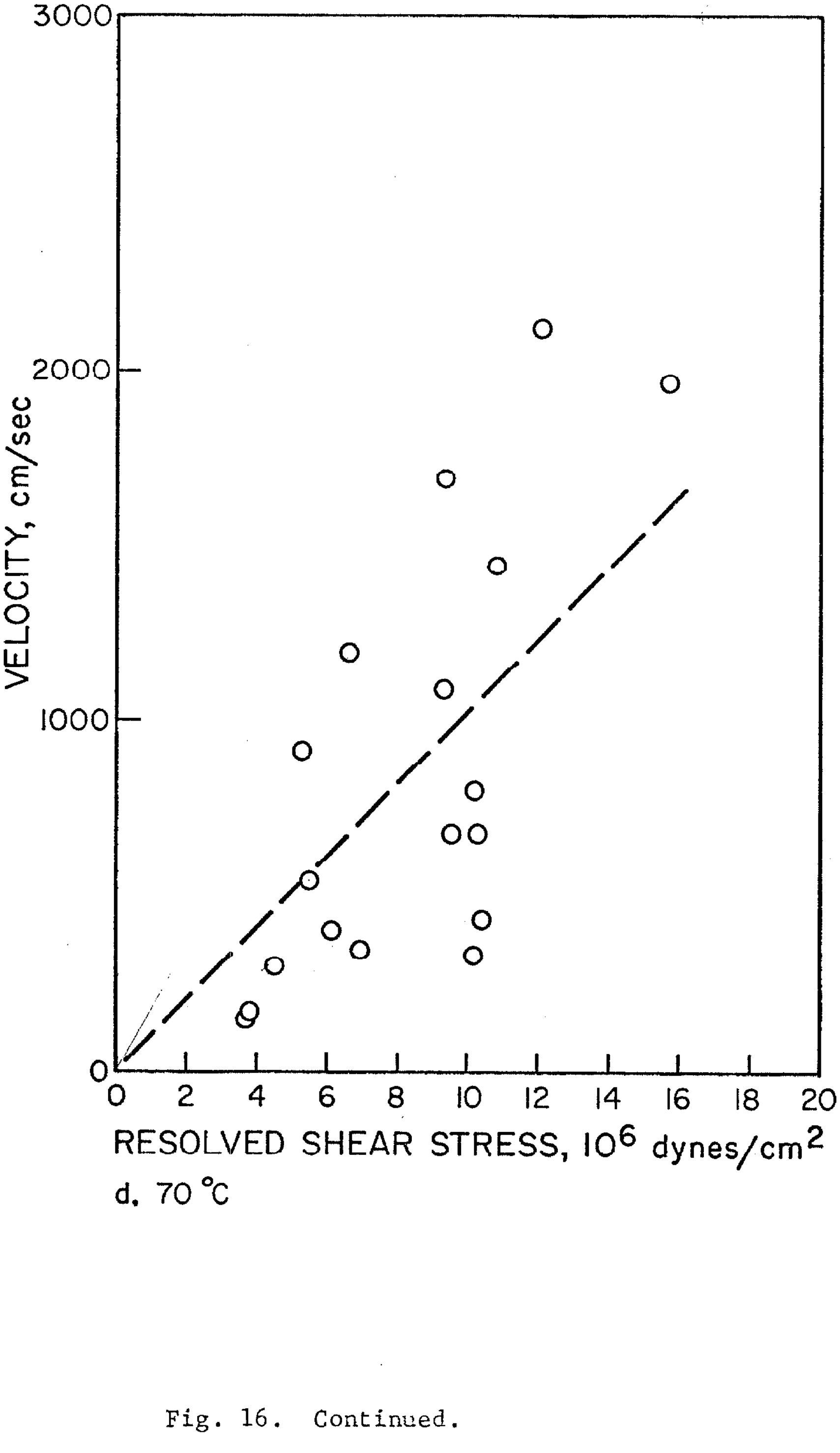

Fig. 16. Continued.

the scatter in the data did not seem to warrant more precise fits.

Dislocation Drag Coefficient

If the velocity is linearly proportional to the stress, the velocity-stress relationship can be represented by the use of a viscous drag coefficient B. The force F per unit length on a dislocation due to the applied resolved shear stress τ_r is

$$F = \tau_r b \quad [8]$$

where b is the Burgers vector of the dislocation. During steady motion this force is considered to be balanced by a viscous drag force, so that

$$F = \tau_r b = Bv \quad [9]$$

where B is the drag coefficient and v is the dislocation velocity. Solving for B one obtains:

$$B = \frac{\tau_r}{v} b \quad [10]$$

The drag coefficient B obtained in this experiment is plotted as a function of temperature in Figure 17. It can be seen that the viscous drag decreases as temperature decreases, which means that dislocation velocity for the same stress will increase as temperature decreases.

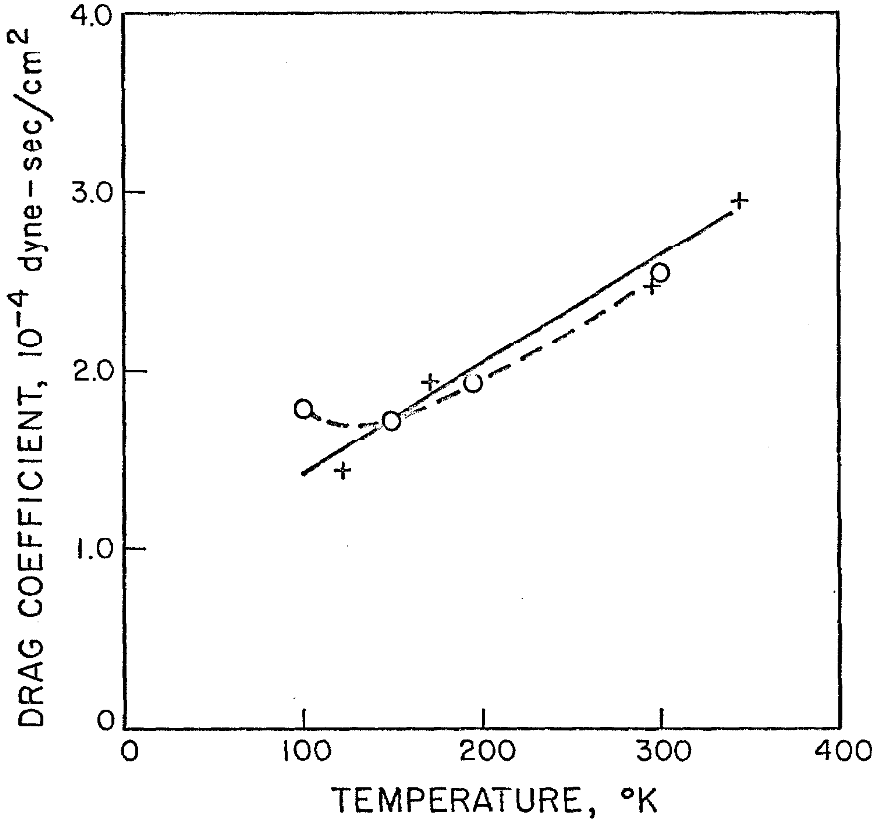

NOTES: 1. SOLID LINE AND + DATA POINTS ARE FROM THIS EXPERIMENT.

2. DASHED LINE AND O DATA POINTS ARE FROM INTERNAL FRICTION MEASUREMENTS (5) BASED ON AN ASSUMED DENSITY OF MOBILE DISLOCATIONS OF 1.2×10^6 cm/cm^3

Fig. 17. Dislocation Drag Coefficient vs Temperature.

V. DISCUSSION

Effect of Line Tension

The line tension of a dislocation can reduce the net force on the dislocation if the dislocation is curved. The line tension of a dislocation is commonly estimated as Gb^2 (23), where G is the modulus of rigidity and b is the Burgers vector. The resolved shear stress τ required to maintain a dislocation with a radius of curvature r in equilibrium is

$$\tau = \frac{Gb}{r} \qquad [11]$$

A typical radius of curvature of the dislocations in a tested specimen is 0.03 cm. The stress required to maintain this radius is about 0.2×10^6 dynes/cm^2, a small stress compared to the applied stresses in this work. Therefore, it is concluded that the influence of the curvature of the dislocations upon their velocity, in this investigation, was negligible.

The typical visible length of segments of dislocation line in the Berg-Barrett X-ray micrographs was 0.02 cm. At the locations where the dislocation becomes invisible the dislocation line might continue at right angles to the visible segment. This would produce a retarding force of about $2Gb^2$, which would balance an applied stress of 0.7×10^6 dynes/cm^2, a small stress compared to applied stresses in this investigation. Therefore, it is concluded that this effect was negligible.

Effect of Dislocation Interactions

The stress fields of nearby dislocations on the same slip plane can change the effective stress acting on a dislocation. The dislocation furthest from the scratch or line of laser damage is typically about 0.002 cm from the nearest dislocation, both before and after testing. Assuming that the dislocations lie on the same slip plane and are edge dislocations, the interaction stress would be about 0.8×10^6 dynes/cm^2. This is a small stress compared to the applied stress for most data points; therefore, dislocation interaction effects are believed to be small.

Effect of Pinning by Point Defects and Dislocations on Other Slip Planes

The effects of point defects and dislocations on other slip planes cannot be quantitatively assessed. The number of point defects was minimized by the use of 99.999 percent pure material. Diffusion of point defects to dislocations produced by scratches or laser damage is believed to be small since delays varying between one hour and four days between producing the dislocations and torsion testing did not appear to affect the number of dislocations moving or their speed. The effect of dislocations on other slip systems is also believed to be small. Essentially all dislocations in the crystals close enough to the surface to affect the observed dislocations were coalesced into subgrain boundaries by annealing. This was confirmed in several cases by electrolytically removing about 50μ of material from the surface of an annealed crystal and observing the dislocations as revealed in Berg-Barrett X-ray micrographs.

Acceleration Times

The method used to obtain dislocation velocities from the displacement and time duration data assumed that the dislocation motion was in phase with the applied stress. This assumption is reasonable if the dislocation acceleration time is small compared to the stress pulse rise time of about 2 X 10^{-6} seconds.

The effective mass m per unit length of a dislocation is about (23)

$$m = \frac{Gb^2}{c_s^2} \qquad [12]$$

where G is the modulus of rigidity, b the Burgers vector, and c_s the shear wave velocity which equals $(G/\rho)^{1/2}$ where ρ is the mass density. The equation of motion for a dislocation then is

$$m \frac{\partial v}{\partial t} = \tau b - Bv \qquad [13]$$

where τ is the applied resolved shear stress, B is the drag coefficient and v the velocity. Solving for v one obtains

$$v = \frac{\tau b}{B} (1-e^{-Bt/m}) \qquad [14]$$

The acceleration time constant is thus m/B, which for this experiment is on the order of 10^{-11} seconds. This shows that the acceleration time is negligible, and thus that the dislocation velocity was essentially in phase with the applied stress during the applied stress pulses used in this investigation.

Comparison with Other Experimental Results

The drag coefficient for dislocation velocity has been measured by two indirect techniques, internal friction tests (5) and impact shear tests (24). The results obtained by these measurements are shown in Figures 18 and 19.

As noted in reference (5) the internal friction measurements actually determine the ratio B/ρ_m, where B is the drag coefficient and ρ_m is the density of mobile dislocations. The measured values of B shown in Figure 18 are based on an assumed density of mobile dislocations of 8×10^6 cm/cm^3. The difference in magnitude of the drag coefficient as obtained by internal friction measurements and in the present experiment is not meaningful, since ρ_m is very uncertain. However, the temperature dependence of B as determined by the internal friction measurements agrees quite well with the results of this experiment, as can be seen in Figure 17. The values of B from the internal friction measurements shown in Figure 17 were obtained by using a value for ρ_m of 1.23×10^6 cm/cm^3.

The drag coefficient obtained from the impact shear tests (24) was determined as follows:

1. Small test crystals were deformed in shear in an impact test. From the stress-time records, the shear stress and strain rate were deduced. Tests were performed at a variety of stress levels and temperatures. The data obtained are reproduced in Figure 20.

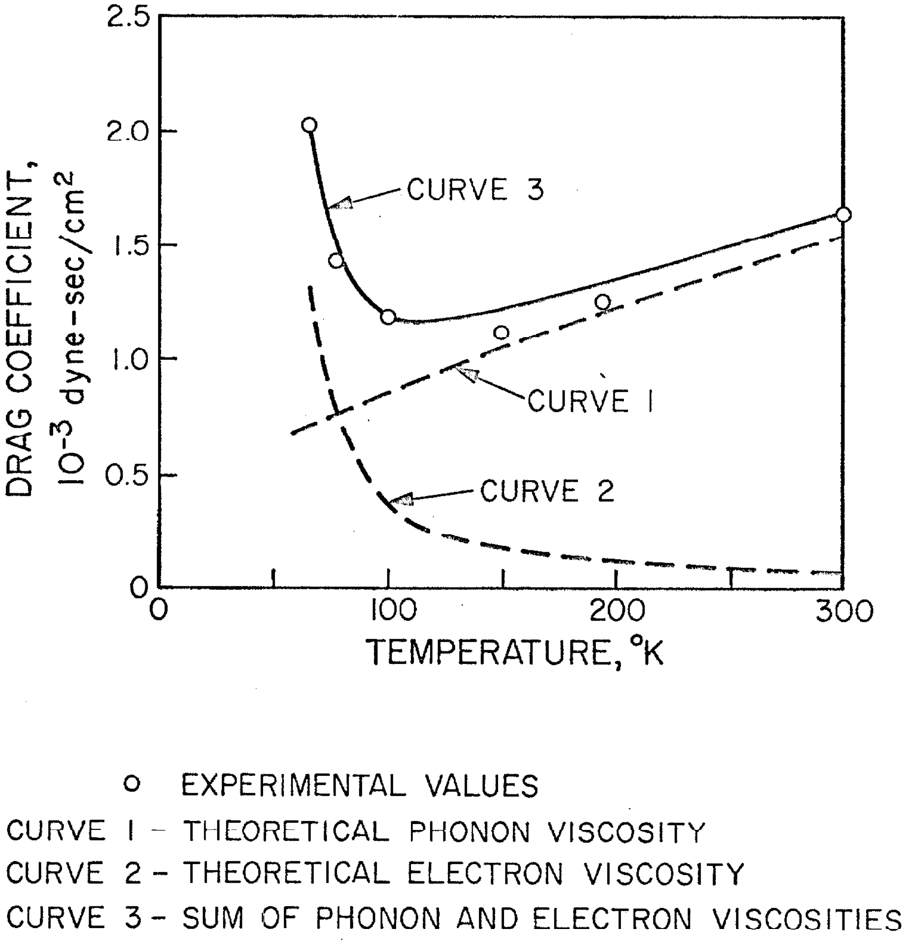

Fig. 18. Dislocation Drag Coefficient vs Temperature from Internal Friction Tests, Mason and Rosenberg (5).

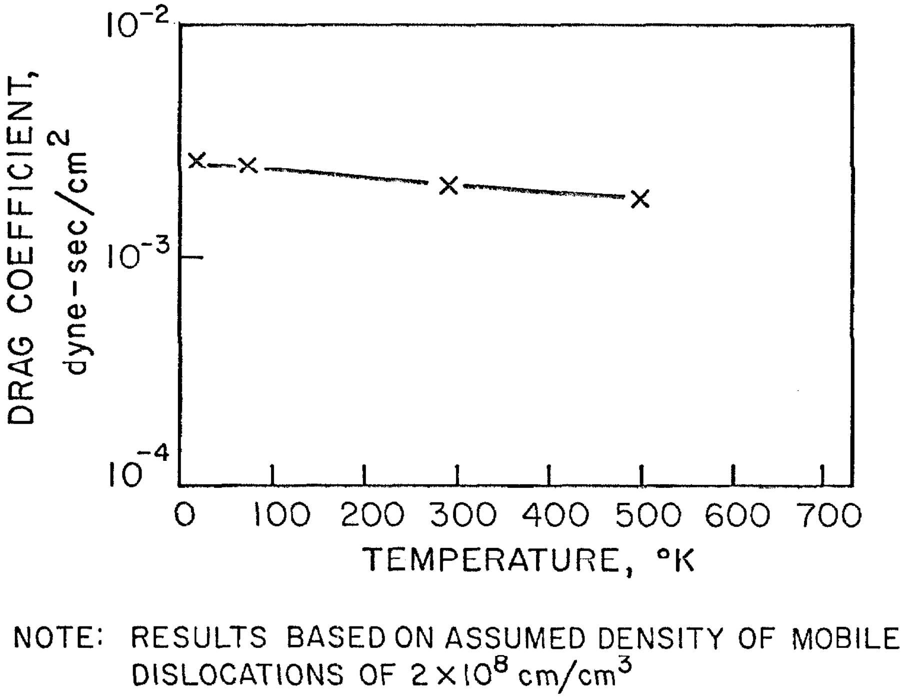

Fig. 19. Dislocation Drag Coefficient vs Temperature from Impact Shear Tests, Ferguson, Kumar and Dorn (24).

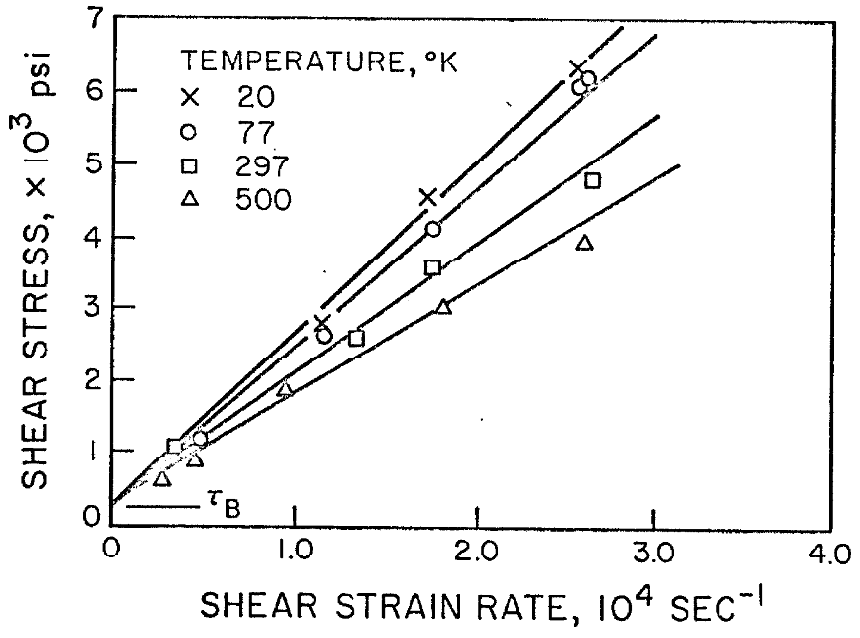

NOTE: FROM Ferguson, Kumar, AND Dorn (24)

Fig. 20. Shear Stress vs Strain Rate from Impact Shear Tests.

2. The shear stress-strain rate data were fitted with the formula

$$\tau - \tau_B = \tau_{eff} = \alpha \dot{\gamma} \qquad [15]$$

where τ is the applied shear stress, τ_B is a back stress defined in Figure 20, τ_{eff} is the effective shear stress, $\dot{\gamma}$ is the strain rate, and α is selected to fit the data.

3. The drag force on a moving dislocation is set equal to the effective applied force:

$$Bv = \tau_{eff} b \qquad [16]$$

where B is the drag coefficient, v the dislocation velocity, and b the Burgers vector. Equation [1] from the introduction was

$$\dot{\gamma} = \rho_m b \bar{v} \qquad [1]$$

Where ρ_m is the density of mobile dislocations and $\bar{v}$ is the average velocity of mobile dislocations. If v of equation [16] and $\bar{v}$ of [1] are assumed to be the same, then equations [15], [16] and [1] reduce to

$$B = \rho_m b^2 \alpha \qquad [17]$$

4. Using equation [17], values of B were obtained using α determined as discussed above and by assuming a value of ρ_m of 2×10^8 cm/cm^3.

The drag coefficient as determined by the impact tests, which is shown in Figure 19, is greater in magnitude than that determined in this experiment. Also, it shows the opposite temperature dependence when compared to the results of this experiment and the internal friction tests cited previously. The magnitude difference in B can be attributed to the unknown value of ρ_m. The opposite temperature dependence, as discussed in reference (24), may be due to dislocations in the shear impact tests interacting with other dislocations or impurities. In addition, the value of ρ_m could vary with temperature, stress, strain or strain rate, and confuse the analysis of the data; for example, as seen from equation [17], a fairly small decrease in ρ_m as temperature is decreased would reverse the temperature dependence of B. It is concluded that the drag coefficient determined by the impact shear tests is not applicable to individual dislocations interacting with the lattice.

Comparison with Theoretical Mechanisms Governing Dislocation Velocities

The theoretical mechanisms governing the velocity of dislocations in relatively pure materials can be divided into two groups, mechanisms which do and do not involve a thermal activation process. In the theories involving thermally activated processes dislocation velocity is considered as being determined by the time required for thermal fluctuations to assist the dislocation to overcome some barrier to motion. The thermally activated mechanisms for governing dislocation velocity, such as interactions of dislocations with point defects (25,26), Peierls barriers (27), and forest dislocations (28) predict rapidly increasing dislocation velocities with increasing temperature since the expression for the velocity contains an exponential term describing the activation process. A thermal activation process clearly does not control dislocation velocities in high purity aluminum single crystals under the conditions in this experiment since the dislocation velocity is found to decrease with increasing temperature.

The proposed mechanisms governing dislocation velocity which do not depend on thermal activation involve interaction of dislocations with electrons and with lattice thermal vibrations. Each of the various theories of this nature which have been proposed will be discussed briefly.

Phonon Viscosity

The development of the phonon viscosity theory given below is based on the work of Mason (29). The quantized lattice vibrations of a crystal can be treated as a gas of phonons. These phonons can interact with each other through the non-linear elastic coupling of atoms in the crystal. The phonon-phonon interactions result in a characteristic relaxation time for phonon energies in different modes of lattice vibration to approach equilibrium.

A shear stress can be resolved into a compressive stress and an orthogonal tension stress. If a step change in shear stress is impressed on a region of a crystal, the radiation pressure of the phonon gas in the compression direction is increased with a corresponding increase in phonon temperature; in the tension direction the radiation pressure and temperature are decreased. These changes in radiation pressure cause an increase in the modulus of rigidity of $E_o/3$, where E_o is the thermal energy density. The increase in the modulus relaxes with a characteristic time, τ, determined by the rate at which phonons of different modes approach equilibrium. As a function of frequency, ω, the modulus of rigidity, G, can be represented by

$$G = G_o + E_o/3 \frac{i\omega\tau}{1+i\omega\tau} \qquad [18]$$

where G_o is the elastic modulus of rigidity determined by slowly applied strains.

The relaxation time τ for phonons is determined by the same processes which are involved in lattice thermal conduction. Using the standard relationships from the kinetic theory of gases one obtains for lattice thermal conductivity and the phonon relaxation time

$$K = \frac{C_v\bar{V}\bar{l}}{3} \qquad \tau = \frac{\bar{l}}{\bar{V}} = \frac{3K}{C_v\bar{V}^2} \qquad [19]$$

where K is the lattice thermal conductivity, C_v the specific heat per unit volume, $\bar{l}$ the phonon mean free path, and $\bar{V}$ the weighted mean phonon velocity.

The relaxation time τ is found to be of the order of 10^{-11} sec. A dislocation strain field has a characteristic width of the order of

10^{-6}cm. The strain in the lattice as a dislocation passes by at a velocity of about 10^3 cm/sec thus experiences a half cycle of strain with a frequency ω of the order of 10^9 cycles per second. Therefore, $\omega\tau$ is much less than unity and equation [18] reduces to

$$G = G_o + \frac{i\omega E_o\tau}{3} \doteq G_o + i\omega\eta \qquad [20]$$

where η is the viscosity of the phonon gas and is given by:

$$\eta = \frac{E_o\tau}{3} = \frac{E_oK}{C_v\bar{V}^2} \qquad [21]$$

The rate of energy dissipation for dislocation motion caused by the phonon viscosity is determined from the integration over the dislocation strain field of the product of the viscosity times the strain rate squared. The rate of energy dissipation $\dot{W}$ per unit length for a screw dislocation is found to be

$$\dot{W} = \frac{b^2v^2\eta}{8\pi a^2} \qquad [22]$$

where b is the Burgers vector, v the dislocation velocity and a the dislocation core radius. The energy dissipation for an edge dislocation is not much different. The energy dissipated by a dislocation per unit length is related to the drag coefficient B by:

$$\dot{W} = v^2B \qquad [23]$$

Using equations [21], [22] and [23] one obtains

$$B = \frac{b^2 \eta}{8\pi a^2} = \frac{b^2}{8\pi a^2} \frac{E_o K}{C_v \bar{V}^2} \qquad [24]$$

The above equation for the drag coefficient was based on the assumption that the material in which the dislocation moved was isotropic. As discussed by Mason and Bateman (30), in a crystalline material the relation between strain and changes in lattice vibration frequency and hence phonon temperature, varies in different directions in the crystal. This effect can result in increased phonon viscosity. To account for this effect equation [24] should be multiplied by a non-linearity constant D, giving

$$B = \frac{b^2 D}{8\pi a^2} \frac{E_o K}{C_v \bar{V}^2} \qquad [25]$$

According to Mason and Bateman (30), the value for the non-linearity constant can be calculated if the third order elastic constants are known. For aluminum, the third order elastic constants are not known and the non-linearity constant has not been evaluated. Mason and Rosenberg (5) estimate that a value of D = 3.95 is necessary to make theoretical values of dislocation damping fit their internal friction data; however, since this fit also depends on their assumed values for dislocation density and dislocation core radius, the value of the non-linearity constant remains uncertain.

In addition to uncertainty in the non-linearity constant, equation [25] for the drag coefficient is also uncertain because of the difficulty of determining the proper values of the dislocation core radius and the lattice thermal conductivity. Mason (29) originally used a core radius of $a = b/6$, but subsequently (31) recommended using $a = (3/4)b$ or $a = v/\tau$ whichever was larger, where v is the dislocation velocity and τ is the phonon relaxation time given in equation [19]. The value of $a = (3/4)b$ is justified by Mason on the basis that it is the limit to which linear elasticity theory holds, and $a = v/\tau$ is justified on the basis that for a radius less than v/τ phonon relaxation will not occur during the transit time of the dislocation core. On the other hand, Lothe (32) considers that $\bar{\ell}$, the phonon mean free path, should be used as the core radius.

If Mason's choice of the core radius or any other constant core radius is used the temperature dependence of the drag coefficient given by [25] is determined by the variation of E_o, K and C_v with temperature. If Lothe's (32) choice of the core radius is used, the value of the drag coefficient becomes, using equation [19] for $\bar{\ell}$:

$$B = \frac{b^2 D E_o C_v}{72\pi K} \qquad [26]$$

which shows a much more rapid fall off with temperature than if a constant core radius is used because C_v decreases and K increases as temperature is decreased.

The temperature dependence of the drag coefficient calculated using a constant dislocation core radius agrees fairly well with the results of this experiment. However, the magnitude of the drag coefficient calculated by Mason and Rosenberg (5) using a core radius of $a = (3/4)b$ and a non-linearity constant $D = 3.95$ is about six times greater than that measured in this experiment. Their theoretical results, using $a = (3/4)b$ and $D = 3.95$, are shown in Figure 18. It appears that in the phonon viscosity theory a constant core radius should be used, but that the value of the core radius must be increased and possibly the non-linearity constant must also be decreased.

<u>Electron Viscosity</u>

The free electron gas in a metal can cause viscous damping of dislocation motion in the same manner as discussed above for the phonon gas (33, 34). The viscosity η of a free electron gas is

$$\eta = \frac{NM\bar{\ell}\bar{v}}{3} \qquad [27]$$

where N is the density of free electrons per unit volume, M is the electron mass, $\bar{\ell}$ is the electron mean free path, and $\bar{v}$ is the average speed of free electrons. Using the average electron velocity for a Fermi distribution of energies, and using the electron mean free path as determined by resistivity measurements, Mason (33) obtains for η

$$\eta = \frac{\hbar^2 (3\pi^2 N)^{2/3}}{5e^2 R} \qquad [28]$$

where $\hbar$ is Plancks constant divided by 2π, e is the electron charge, and R is the resistivity.

The drag on a moving dislocation is then calculated by integrating over the strain field of a moving dislocation as was done above using the phonon viscosity, with the result that the same equation, namely

$$B = \frac{b^2\eta}{8\pi a^2} \qquad [29]$$

holds for the drag coefficient B except that the values used for the viscosity η and core radius a are those appropriate to electron damping. The value of B again is uncertain because of uncertainty in the proper value of the core radius a. Rosenberg and Mason (5) have computed the drag coefficient due to electron viscosity as a function of temperature using equations [28] and [29] together with the assumption that the core radius is about 10^{-7} cm. Their results are shown in Figure 18 together with data from internal friction measurements. The theoretical results and internal friction measurements indicate that at about 100°K the effects of electron viscosity on the drag coefficient should become noticeable. The present experiment did not reach a sufficiently low temperature to test that prediction.

Glide Plane Viscosity

Gilman (35) has proposed that the losses near the dislocation core be calculated using a viscosity such as that due to intermolecular forces acting directly across the glide plane with a finite relaxation time. Gilman shows that if this viscosity is applied to the bulk of the crystal as well as the dislocation core, the viscous losses in the core region will exceed those in the bulk of the crystal by a factor of about eight. Gilman suggests that the value of viscosity η computed by Mason using the phonon viscosity theory is the appropriate value to employ, for metals, in his expression for the drag coefficient, B.

A quantitative analysis of glide plane viscosity cannot be performed since there is as yet no way of estimating an appropriate value of the viscosity. Phonon viscosity is not applicable to the dislocation core since phonon viscosity depends on phonon-phonon interactions and therefore, is not applicable to regions much smaller than the phonon mean free path. Also, if the phonon viscosity value of η were used in Gilman's theory, it would result in a drag coefficient B about 50 times greater than that obtained in the present investigation.

Thermoelastic Effect

Eshelby (36) demonstrated that the compressive and tensile stresses around a moving edge dislocation will cause irreversible heat flow to take place and thus will dissipate energy. Calculations using the equations of Weiner (37) and Lothe (32) show that this effect results in a drag coefficient for aluminum three or more orders of magnitude less than that determined in this experiment. The low rate of energy dissipation in aluminum due to this effect is a result of the high thermal conductivity of aluminum, which makes the compression and tension around the edge dislocation occur in a nearly isothermal manner.

Anharmonic Radiation from the Dislocation Core

The vibrational energy of the atoms in the highly distorted region of the dislocation core will be increased as the dislocation moves because of the anharmonic coupling forces between atoms. The radiation of this energy away from the dislocation contributes to dislocation damping. Lothe (32) has estimated the effect of anharmonic radiation for an edge dislocation and obtained

$$B = \frac{(2\pi)^2}{\bar{V}} \cdot \frac{3\epsilon_o}{nb^2} \; \frac{\epsilon_o e^{h\nu_o/kT}}{kT} \; \left(\frac{\delta\nu}{\nu_o}\right)^2 \qquad [30]$$

where B is the damping coefficient, ϵ_o is the mean thermal energy per atom, n is the number of atoms in the dislocation core width, b is the Burgers vector, ν_o is the frequency of vibration of an atom in an undisturbed region of the crystal, $\delta\nu$ the change in frequency of an atom in the dislocation core relative to ν_o, $\bar{V}$ is the weighted mean speed of sound, k is Boltzmann's constant and T is the absolute temperature.

Using a dislocation core width of $n = 5$, a frequency change of $\frac{\delta\nu}{\nu_o} = 1/10$, a thermal energy density of $E_o = 3\ \epsilon_o/b^3$, and assuming that at high temperatures $\frac{\epsilon_o e^{h\nu_o/kT}}{kT} \approx 1$, Lothe obtains

$$B = \frac{E_o b}{12\bar{V}} \qquad [31]$$

The value obtained by Lothe is uncertain because of the difficulties in estimating the appropriate frequency change and core width. The frequency change is difficult to estimate since it is a function of the anharmonic terms in the atom coupling and is sensitive to the actual atomic arrangement in the dislocation core.

Equation [31] gives a value of the drag coefficient at room temperature about an order of magnitude lower than that measured in this experiment. In addition, the value of the drag coefficient given by equation [31] decreases more rapidly as temperature decreases than does the experimental drag coefficient.

Phonon Scattering

The various mechanisms by which dislocation damping can be caused by phonon scattering have been reviewed by Lothe (32). At temperatures below the Debye temperature for materials with a negligible Peierls barrier such as aluminum, there are two significant phonon scattering mechanisms. The first mechanism is the scattering of phonons by the dislocation strain field in a manner analogous to the refraction of light. The second mechanism is the absorption of energy from phonons by the dislocation and subsequent vibration of the dislocations with re-radiation of phonons.

The dislocation strain field affects phonons through the anharmonic coupling of the atoms, which results in a scattering probability for an incident phonon. A stationary dislocation in an isotropic flux of phonons will thus have a symetric energy flux per unit time $\dot{W}$ per unit length scattered from it. If the dislocation is moving with a velocity u, the scattered phonon radiation is asymetric and gives off a net amount of quasi-momentum $\frac{\dot{W}u}{\bar{V}^2}$ per unit length, where $\bar{V}$ is the weighted average velocity of phonons. This results in a drag coefficient B of

$$B = \frac{\dot{W}}{\bar{V}^2} \qquad [32]$$

Using rather uncertain estimates for the scattering probability to evaluate $\dot{W}$ Lothe (32) finds that the drag coefficient from strain field scattering will be

$$\frac{E_o b}{60\bar{V}} < B < \frac{E_o b}{5\bar{V}} \qquad [33]$$

where E_o is the thermal energy density and b is the Burgers vector. It should be noted that the drag coefficient due to this mechanism will decrease faster with temperature than the thermal energy density since the scattering probability will decrease as the average phonon energy decreases.

Phonon scattering by induced vibrations of the dislocation has been considered by several authors, Leibfried (38), Nabarro (39), Eshelby (40) and Lothe (32, 41). This mechanism again results in a symetric flux of scattered radiation for a stationary dislocation, and makes use of equation [32] to obtain the drag coefficient. Lothe (32) obtained for this mechanism:

$$B \approx (1/16\bar{V}) \int_0^{q_{max}} \epsilon \, q \, dq \qquad q_{max} = \frac{\pi}{b} \tag{34}$$

where B is the drag coefficient, q is the phonon wave vector, $\bar{V}$ is average speed of sound, and ϵ is the average energy of a thermal wave given by

$$\epsilon(\omega,T) = \frac{\hbar\omega}{e^{\hbar\omega/kT} - 1} \qquad \omega = \bar{V}q \tag{35}$$

where ω is the frequency, T the absolute temperature, and k is Boltzmanns constant. In the high temperature limit $\epsilon(\omega,T) \approx kT$ and the thermal energy density is $E_o \approx \frac{3kT}{b^3}$ where b is the Burgers vector, and the damping coefficient becomes

$$B \approx \frac{E_o b}{10\bar{V}} \tag{36}$$

The drag coefficient from both types of phonon scattering is then about

$$B \approx \frac{E_o b}{5\bar{V}} \tag{37}$$

The magnitude of this drag coefficient at room temperature is about one fourth of the experimental value, and it decreases with decreasing temperature more rapidly than the experimental value.

This comparison of theory with the results of the present experiment indicates that the thermoelastic effect is negligible compared to the other mechanisms, and that the glide plane viscosity theory is difficult to quantitatively evaluate but tentatively appears to predict too large a dislocation damping. The electron viscosity mechanism may contribute to the low temperature damping; however, the magnitude of the effect was too low to be detected in the test temperature range of the present investigation. Anharmonic radiation and phonon scattering may contribute significantly to dislocation damping at higher temperatures (room temperature and above) but phonon viscosity appears to be the predominant damping mechanism governing the mobility of glide dislocations on the (111) planes in aluminum in the temperature range -150°C to 70°C. This conclusion is based on:

1. The phonon viscosity theory using a constant dislocation core radius predicts a drag coefficient decreasing more slowly with decreasing temperature than the thermal energy density while the anharmonic radiation theory and the phonon scattering theories predict a drag coefficient decreasing as fast or faster than the thermal energy density. Figure 21 shows the dislocation drag coefficient, B as a function of absolute temperature as determined by
   a) results of the present experiment
   b) phonon viscosity theory using values for the non-linearity constant and core radius selected to give a good fit with the results of this experiment.

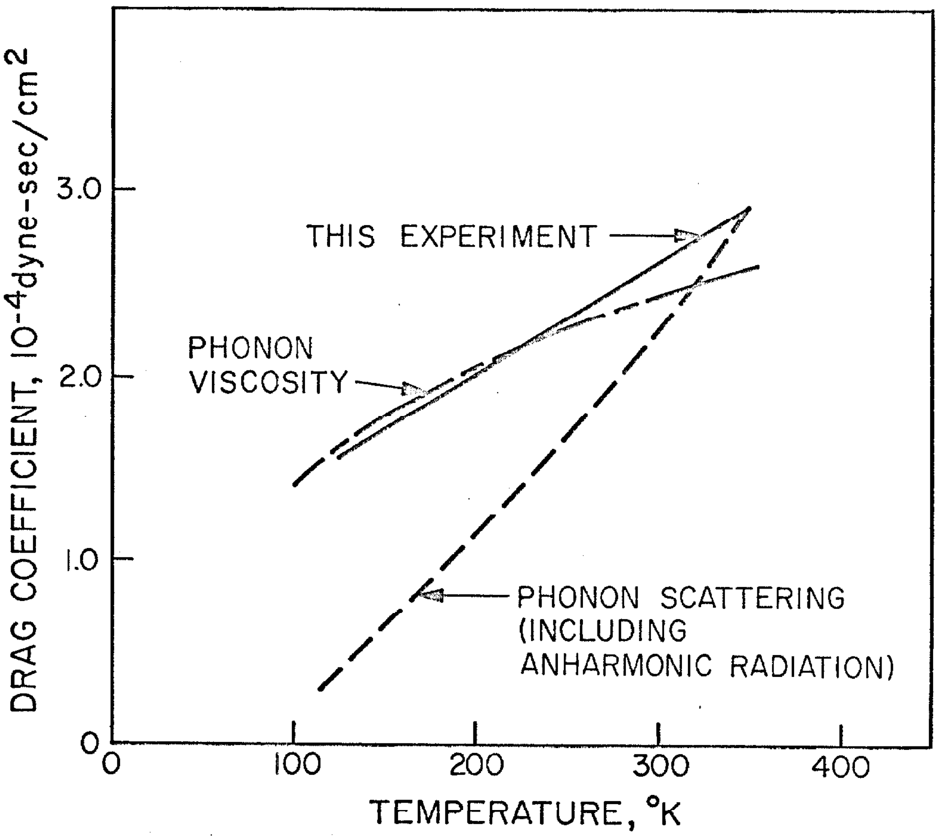

NOTES: 1. PHONON VISCOSITY CURVE BASED ON A NON-LINEARITY CONSTANT OF UNITY AND A DISLOCATION CORE RADIUS OF 0.95 b, DEBYE THEORY SPECIFIC HEAT AND ENERGY DENSITY, THERMAL CONDUCTIVITY FROM MASON AND ROSENBERG (5), AND $\bar{V} = 3.5 \times 10^5$ cm/sec.

2. PHONON SCATTERING CURVE IS FROM $B = 0.64\, E_0 b/\bar{V}$, WHERE THERMAL ENERGY DENSITY IS FROM THE DEBYE THEORY AND $\bar{V} = 3.5 \times 10^5$ cm/sec.

Fig. 21. Theoretical and Experimental Values of Dislocation Drag Coefficient vs Temperature.

c) phonon scattering and anharmonic radiation theory with constants selected to give agreement with the results of this experiment at 350°K.

Figure 21 shows that the drag coefficient, B, from the phonon viscosity theory and the experimental results have about the same temperature dependence, while the drag coefficient from the phonon scattering and anharmonic radiation theory decreases too rapidly as temperature is decreased. Electron viscosity effects (5), if added to the phonon scattering and anharmonic radiation results, are not sufficiently great to correct the temperature dependence discrepancy of the phonon scattering theory.

2. The magnitude of the dislocation drag coefficient predicted by the phonon viscosity theory is about 6 times greater than the experimental value. This is not significant, however, considering the uncertainties in the dislocation core radius, non-linearity constant and lattice thermal conductivity. The magnitude of the sum of the phonon scattering and anharmonic radiation theories is about 3 times too small; though again this is probably not significant considering uncertainties in the theories.

VI. SUMMARY AND CONCLUSIONS

Dislocations of edge and mixed character were produced within a depth of about 10μ below the (111) test surface of 99.999% purity aluminum single crystals by scratching and by damaging with laser pulses. Movement of these dislocations on the (111) glide planes parallel to the test surface was produced by resolved shear stresses ranging from 0.5 to 16 X 10^6 dynes/cm^2 applied to the test surface for periods ranging from 15 to 108 μsec. Tests were performed in the temperature range -150°C to 70°C. Dislocation displacement was measured using the Berg-Barrett X-ray technique.

Dislocation velocity determined from the test data at each test temperature was approximately linearly proportional to the applied resolved shear stress. Dislocation velocity increased as temperature decreased at the same stress. The dislocation drag coefficient ranged from $1.5X10^{-4}$dyne-sec/cm^2 at -150°C to $2.9X10^{-4}$dyne-sec/cm^2 at 70°C. The variation of dislocation velocity with stress and with temperature agrees approximately with the predictions of the phonon viscosity theory (5,29,30). The theory predicts somewhat lower velocities than those observed, however. This discrepancy may result from uncertainty in the appropriate dislocation core radius and non-linearity constant to use in the theory. Phonon scattering and anharmonic radiation of phonons from the dislocation core (32) may also contribute significantly to limiting dislocation velocity, particularly in the higher temperature portion of the test range. The glide plane viscosity theory (35) predicts dislocation velocities much lower than those observed and thus does not appear to be the mechanism governing dislocation velocity under the conditions of the present investigation.

APPENDIX A

The Propagation of an Elastic Torsion Wave Along the [111] Axis of an Aluminum Single Crystal.

The stress distribution associated with an elastic torsion wave in an aluminum single crystal may differ from the simple stress distribution for torsion of an isotropic material given by the elementary theory of elasticity due to the anisotropy in the elastic properties of aluminum single crystals. The purpose of this analysis is to estimate the magnitude of this effect in the case when the torsion wave propagates along a circular cylindrical rod whose axis is parallel to the [111] direction of the crystal structure. This is accomplished by assuming that the displacements associated with the torsion wave are the same as those in the elementary theory (the cross sections normal to the axis rotate as rigid bodies and do not warp) and calculating the stresses produced by such a deformation.

The stiffness moduli for [111] oriented aluminum are tabulated in reference (33) and are:

$$C_{11} = 10.82 \text{ X } 10^{11} \text{ dynes/cm}^2$$

$$C_{12} = 6.13 \text{ X } 10^{11} \text{ dynes/cm}^2$$

$$C_{44} = 2.85 \text{ X } 10^{11} \text{ dynes/cm}^2$$

These stiffness moduli must be transformed into the set of constants appropriate to a [111] axis single crystal. This transformation is carried out in Appendix A of reference (10) and will not be duplicated here. The relation of the original set of coordinate axes and the new set of coordinate axes is shown in Figure A-1. Coordinate axis X_1' is aligned with the [111] axis of the crystal, while coordinate axes X_2' and X_3' are radial lines in the plane perpendicular to the crystal axis, i.e. in the (111) slip plane. The effect of angular position about the cylinder axis on the stress can be determined by varying the angular position of the coordinate axes X_2' and X_3'.

As discussed earlier, we assume that a pure twisting motion is applied. We align the coordinate axes so that this results in ϵ_5' being the only strain. Using the transformed elastic constants developed in reference (10),we have as the resulting stress state:

$$\sigma_1' = 0$$

$$\sigma_2' = \frac{C\cos\theta}{3\sqrt{2}} (1 - 2 \cos 2\theta)\epsilon_5'$$

$$\sigma_3' = \frac{-C\cos\theta}{3\sqrt{2}} (1 - 2 \cos 2\theta)\epsilon_5'$$

$$\sigma_4' = \frac{C\sin\theta}{3\sqrt{2}} (1 + 2 \cos 2\theta)\epsilon_5'$$

$$\sigma_5' = (\frac{1}{3} C + C_{44})\epsilon_5'$$

$$\sigma_6' = 0$$

where the angular position θ is defined in Figure A-1 and C is defined by

$$C = C_{11} - C_{12} - 2C_{44}$$

Evaluating the stresses using the elastic constants for aluminum shows that the maximum values of σ_2', σ_3' and σ_4' are all less than ten percent of the radial shear stress σ_5'. The low values of the σ_2', σ_3' and σ_4' indicate that the [111] axis aluminum is behaving in a nearly

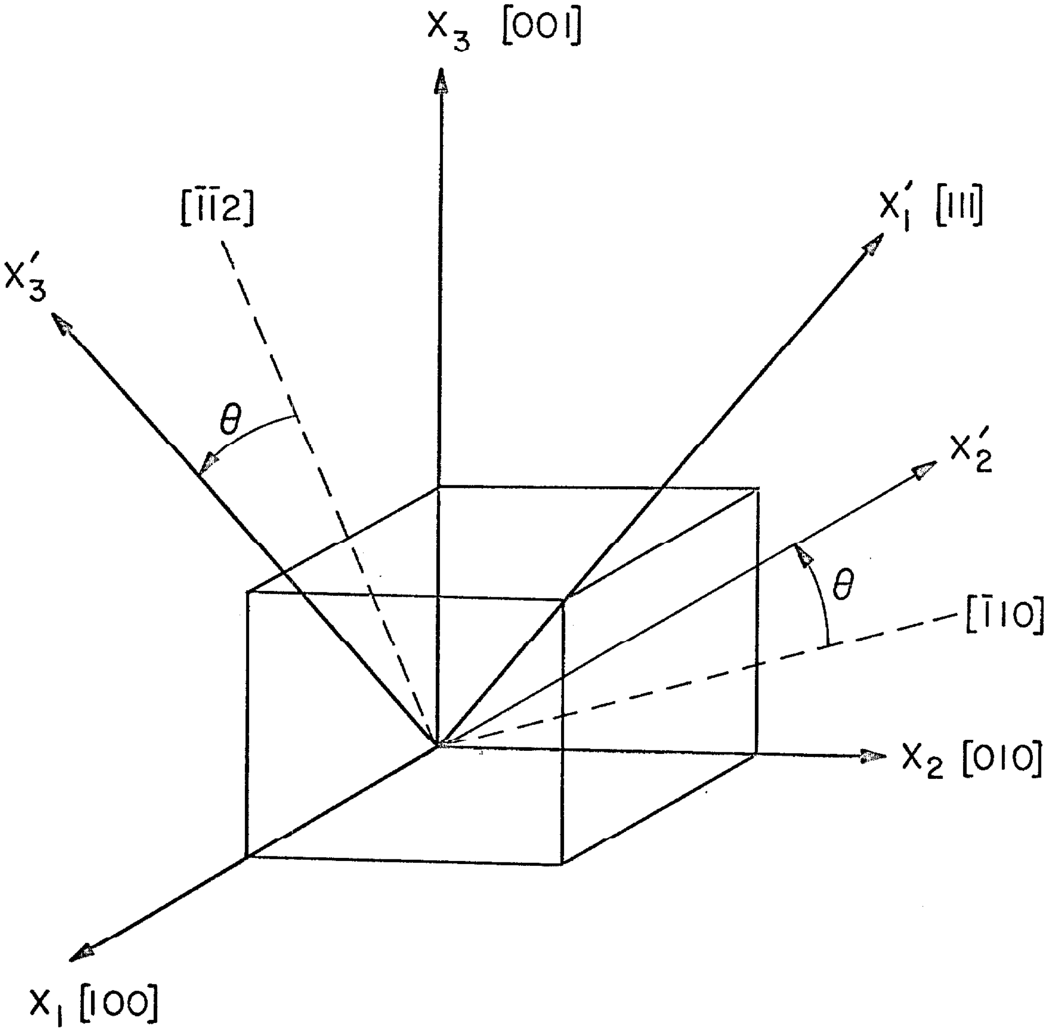

Fig. A-1. Coordinate Axes Transformation isotropic manner since the elementary theory predicts that the only stress would be σ_5'. Therefore, the stress state calculated using the elementary theory of elasticity is a reasonable approximation of the actual stress state.

APPENDIX B

Transmission of Elastic Torsion Waves Along a Cylindrical Bar Containing a Gap with a Low Modulus Elastic Material.

The purpose of this analysis is to estimate the effect of a gap filled with a low modulus material on the rise time of a torsion stress wave travelling along a cylindrical bar. Consider an incident torsion wave travelling in the positive x direction as shown in Figure B-1. Assume completely elastic behavior so that the following equations hold:

$$\tau = \frac{T\ r}{J} \qquad [B1]$$

$$\Delta\tau = \rho\ C\ \Delta v \qquad [B2]$$

where τ is the shear stress, T is the torque, r is the radius, $J = \frac{\pi\ r^4}{2}$ is the polar moment of inertia, ρ is the density, $C = (G/\rho)^{1/2}$ is the shear wave speed, G is the modulus of rigidity, $v = \frac{d\varphi}{dt}\ r$ is the particle velocity, and $\frac{d\varphi}{dt}$ is the angular velocity.

The boundary conditions between regions I, II and III of the rod are

1. Continuity of torque. Because of equation [B1], this leads to continuity of stress, $\tau_I = \tau_{II}$ at x_1, $\tau_{II} = \tau_{III}$ at x_2.
2. Continuity of particle velocity, $v_I = v_{II}$ at x_1, $v_{II} = v_{III}$ at x_2.

where Roman numeral subscripts refer to regions of the rod. Arabic

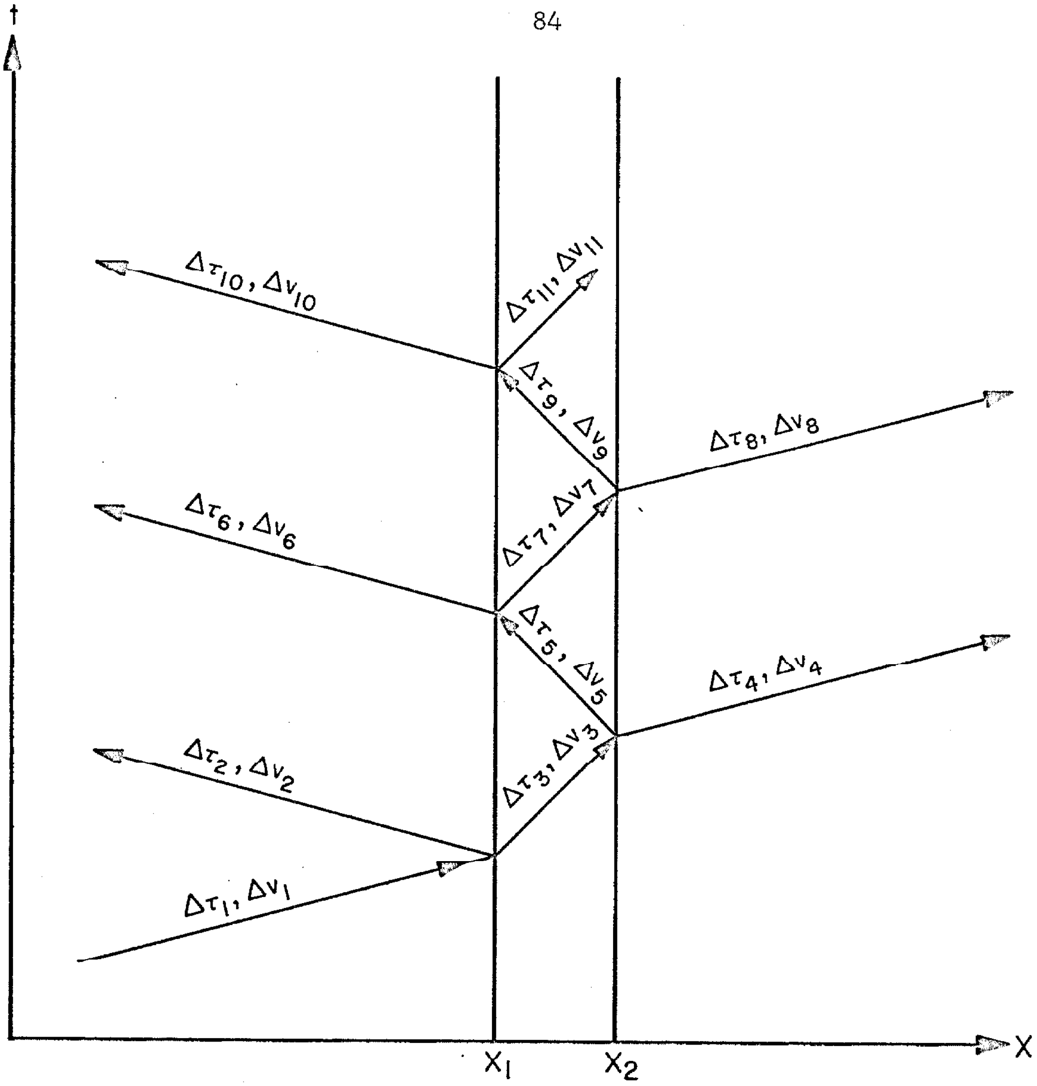

STRESS WAVE TIME-POSITION DIAGRAM

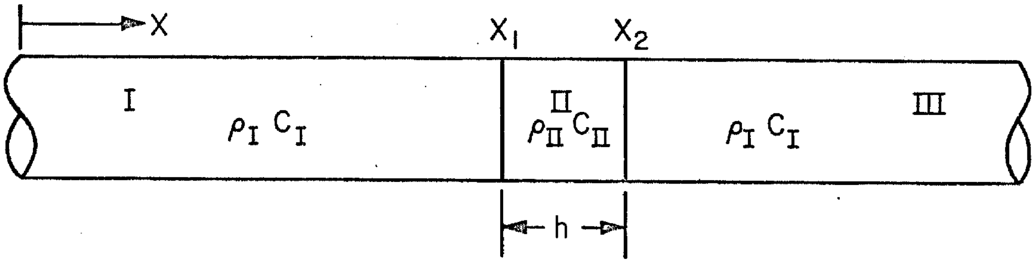

ROD WITH GAP

Fig. B-1. Torsion Stress Pulse Transmission Across a Low Modulus Gap.

numeral subscripts are used to identify waves as shown in Figure B-1.

Continuity of stress requires

$$\Delta\tau_1 + \Delta\tau_2 = \Delta\tau_3 \qquad [B3]$$

Continuity of particle velocity requires

$$\Delta v_1 + \Delta v_2 = \Delta v_3 \qquad [B4]$$

Substituting equation [B2] into [B4], and recognizing that $\Delta\tau_2 = - \rho_I C_I \Delta v$ since the wave is travelling in the negative direction, gives

$$\frac{\rho_{II} C_{II}}{\rho_I \; C_I} (\Delta\tau_1 - \Delta\tau_2) = \Delta\tau_3 \qquad [B5]$$

Solving equations [B3] and [B5] for $\Delta\tau_2$ gives

$$\Delta\tau_2 = \frac{- \Delta\tau_1 (1 - \frac{\rho_I \; C_I}{\rho_{II} C_{II}})}{(1 + \frac{\rho_I \; C_I}{\rho_{II} C_{II}})}$$

The remaining stress waves shown on Figure B-1 can be obtained in a similar manner. Letting $\frac{\rho_{II} C_{II}}{\rho_I \; C_I} = \alpha$ the stress waves are:

Stress Wave	Value
$\Delta\tau_1$	$\Delta\tau_1$
$\Delta\tau_2$	$-\Delta\tau_1 \frac{(1 - \alpha)}{(1 + \alpha)}$
$\Delta\tau_3$	$2\alpha \, \Delta\tau_1 \frac{1}{(1 + \alpha)}$
$\Delta\tau_4$	$4\alpha \, \Delta\tau_1 \frac{1}{(1 + \alpha)^2}$

$\Delta\tau_5$	$2\alpha\ \Delta\tau_1 \dfrac{(1-\alpha)}{(1+\alpha)^2}$
$\Delta\tau_6$	$4\alpha\ \Delta\tau_1 \dfrac{(1-\alpha)}{(1+\alpha)^3}$
$\Delta\tau_7$	$2\alpha\ \Delta\tau_1 \dfrac{(1-\alpha)^2}{(1+\alpha)^3}$
$\Delta\tau_8$	$4\alpha\ \Delta\tau_1 \dfrac{(1-\alpha)^2}{(1+\alpha)^4}$
$\Delta\tau_9$	$2\alpha\ \Delta\tau_1 \dfrac{(1-\alpha)^3}{(1+\alpha)^4}$

etc.

It can be seen that subsequent transmitted waves in rod III will be:

$$\underset{n \geq 1}{\Delta\tau_{4n}} = 4\ \alpha\ \Delta\tau_1 \frac{(1-\alpha)^{2n-2}}{(1+\alpha)^{2n}} = \frac{4\ \alpha\ \Delta\tau_1}{(1-\alpha)^2} \left[\frac{1-\alpha}{1+\alpha}\right]^{2n} \qquad [B6]$$

and subsequent reflected waves will be:

$$\underset{n \geq 1}{\Delta\tau_{4n+2}} = 4\ \alpha\ \Delta\tau_1 \frac{(1-\alpha)^{2n-1}}{(1+\alpha)^{2n+1}} \qquad [B7]$$

The first reflected wave, $\Delta\tau_2$, is an unloading wave while the subsequent reflected waves are loading waves tending to restore the stress in rod I to the original value of $\Delta\tau_1$. The transmitted waves are all loading waves tending to build up the stress in rod III to $\Delta\tau_1$.

Using the standard formula for the sum of a geometric progression, the sum of the first N transmitted waves is found to be:

$$\sum_{n=1}^{N} \Delta\tau_{4n} = \Delta\tau_1 \left[1 - \left(\frac{1-\alpha}{1+\alpha}\right)^{2N}\right] \qquad [B8]$$

The criteria for the gap to pass a torsion stress wave successfully is that a large fraction f be transmitted within the desired rise time Δt. To transmit a fraction f of the incident wave, requires N transmitted waves where:

$$f = \frac{\sum_{n=1}^{N} \Delta\tau_{4n}}{\Delta\tau_1} = 1 - \left(\frac{1-\alpha}{1+\alpha}\right)^{2N} \qquad [B9]$$

Solving for N gives

$$N = \frac{1}{2} \frac{\ln(1-f)}{\ln\left(\frac{1-\alpha}{1+\alpha}\right)} \qquad [B10]$$

The time for the transmitted wave to build up to a value of $f\Delta\tau_1$ is thus seen to be, using Figure B-1, the time required for 2N stress waves to cross the gap. Setting this time equal to the desired rise time gives

$$\Delta t = \frac{2\,N\,h}{C_{II}} \qquad [B11]$$

Solving for the required shear wave speed in the gap, and using equation [B10], gives

$$C_{II} = \frac{2\,N\,h}{\Delta t} = \frac{h}{\Delta t} \frac{\ln(1-f)}{\ln\left(\frac{1-\alpha}{1+\alpha}\right)} \qquad [B12]$$

Equation [B12] relates the required material properties, i. e.

$C_{II} = (G_{II}/\rho_{II})^{1/2}$, with the desired stress pulse rise time Δt and the fraction of the stress wave passed during the rise time, f. For a gap material having a low elastic modulus, α will be much less than unity, and equation [B12] reduces to

$$G_{II} = - \frac{\rho_I C_I}{2} \frac{h}{\Delta t} \ln(1 - f) \qquad [B13]$$

For example, if $h = .0025$ cm, $\Delta t = 10^{-6}$ sec, $f = 0.9$, and $\rho_I C_I = 8.4X10^{-5}$ gm/ cm^2- sec (typical for aluminum), then G_{II} must be more than $2.4X10^9$ dynes/cm^2.

In conclusion, it appears that a modulus of rigidity of about 10^9 dynes/cm^2 is required to pass a torsion wave with a rise time of about a μsec across a thin, .0025 cm, gap. From equation [B13], it can be seen that the rise time Δt is inversely proportional to the modulus of rigidity G; if the modulus is decreased, the time taken to pass a given percentage of the stress across the gap increases proportionately. Also, if the gap height h is increased, the time taken to pass a given percentage of the stress increases proportionately.

APPENDIX C

Demonstration That Dislocation Velocity is Linearly Proportional to Resolved Shear Stress (43).

The purpose of this analysis is to show that the dislocation velocity is linearly proportional to resolved shear stress if the elementary elastic stress distribution for torsion applies and if it is observed that the dislocation displacement, D, is linearly proportional to the product of the radius and the stress resolution factor, rcos θ.

The displacement of a dislocation is given by

$$D = \int_0^\infty v(t)\,dt \qquad [C1]$$

where v(t) is the dislocation velocity and t is the time. Assume that the velocity is some monotonically increasing function of resolved shear stress, τ_r:

$$v = f(\tau_r) \qquad [C2]$$

Assume that the shear stress acting on the test surface is linearly proportional to the radius, i. e. that the elementary elastic stress distribution applies:

$$\tau(r,t) = K \frac{r}{a} S(t) \qquad [C3]$$

where r is the radius, a is the outer radius of the specimen, S(t) is the strain gage record, and K is a constant involving the moment of inertia and the elastic constant.

The resolved shear stress τ_r then is

$$\tau_r = \tau\cos\theta \qquad [C4]$$

where θ is the angle between the perpendicular to the radial line through the dislocation and the Burgers vector of the dislocation.

Using equations [C3] and [C4] the resolved shear stress is

$$\tau_r = K\cos\theta \, \frac{r}{a} \, S(t) \qquad [C5]$$

Equations [C1] and [C2] give for the displacement

$$D = \int_0^\infty f(\tau_r)\,dt \qquad [C6]$$

Differentiating the displacement with respect to rcos θ gives

$$\frac{\partial D}{\partial(r\cos\theta)} = \int_0^\infty \frac{\partial f(\tau_r)\,dt}{\partial(r\cos\theta)} = \int_0^\infty \frac{df(\tau_r)}{d\tau_r} \, \frac{\partial\tau_r}{\partial(r\cos\theta)} \, dt \qquad [C7]$$

Using [C5] in [C7] gives

$$\frac{\partial D}{\partial(r\cos\theta)} = \frac{K}{a} \, \frac{df(\tau_r)}{d\tau_r} \int_0^\infty S(t)\,dt \qquad [C8]$$

The experimental measurements have shown (Figure 14) that the displacement is linearly proportional to rcos θ for a given test, therefore:

$$\frac{\partial D}{\partial(r\cos\theta)} = C_1 = \text{Constant} \qquad [C9]$$

Also, for a given test,

$$\int_0^\infty S(t)\,dt = C_2 = \text{Constant} \qquad [C10]$$

Combining equations [C8], [C9] and [C10] gives

$$\frac{df(\tau_r)}{d\tau_r} = \frac{C_1\,a}{C_2\,K} = C_3 = \text{Constant} \qquad [C11]$$

Integrating [C11] gives

$$v = f(\tau_r) = C_3\tau_r + C_4 \qquad [C12]$$

Assuming that the velocity is zero for a zero stress results in $C_4 = 0$ and gives

$$v = C_3\tau_r \qquad [C13]$$

which shows that the velocity is linearly proportional to the resolved shear stress.

APPENDIX D

Affect of Plastic Yielding on the Stress Distribution in a Cylinder under Torsion.

The purpose of this calculation is to show that plastic yielding in the outer regions of the test specimen did not significantly alter the stress distribution in the inner elastic regions where dislocation velocity was measured. The conservative assumption is made that the material behaves in an elastic - perfectly plastic manner.

The elastic stress distribution τ_{el} in a cylinder to which a torque T is applied is given by

$$\tau_{el} = \frac{2Tr}{\pi a^4} \qquad [D1]$$

where r is the radius and a is the outer radius.

An elastic - perfectly plastic material is one which has a linear stress - strain relation up to a yield stress τ_y , and a constant stress for any further strain. If a cylinder is made of an elastic - perfectly plastic material, the torque carried by the cylinder when the outer part of it has yielded is given by (42):

$$T = \frac{2\pi\tau_y a^3}{3}\left(1 - \frac{\beta^3}{4}\right) \qquad [D2]$$

where β is the ratio of the radius of the boundary between the elastic region and the plastic region to the outer radius. The stress τ in the elastic region is given by

$$\tau = \tau_y \frac{r}{\beta a} \qquad [D3]$$

Solving equation [D2] for τ_y gives

$$\tau_y = \frac{3T}{2\pi a^3\left(1 - \frac{\beta^3}{4}\right)} \qquad [D4]$$

Equations [D3] and [D4] combine to give

$$\tau = \frac{3Tr}{2\pi a^4 \beta (1 - \frac{\beta^3}{4})} \qquad [D5]$$

Using equations [D1] and [D5], the ratio of the stress in the elastic central region of a plastically yielded cylinder to the stress at the same radius in a cylinder without plastic yielding and carrying the same torque is

$$\frac{\tau}{\tau_{el}} = \frac{3}{4\beta (1 - \frac{\beta^3}{4})} \qquad [D6]$$

Significant plastic yielding involves the motion of large numbers of dislocations. Examination of Berg-Barrett X-ray micrographs showed that dislocation multiplication and motion sufficient to result in significant plastic yielding occurred in the worst case for the outer 20% of the radius. In this worst case, $\beta = 0.8$, and the stress in the central region is increased relative to the elastic case by eight percent.

LIST OF REFERENCES

1. W. G. Johnston and J. J. Gilman, "Dislocation Velocities, Dislocation Densities, and Plastic Flow in Lithium Fluoride Crystals," J. Appl. Phys. 30, 129 (1959).

2. J. C. M. Li, "A Dislocation Mechanism of Transient Creep," Acta Met. 11, 1269 (1963).

3. J. W. Taylor, "Dislocation Dynamics and Dynamic Yielding," J. Appl. Phys. 36, 3146 (1965).

4. W. G. Johnston, "Yield Points and Delay Times in Single Crystals," J. Appl. Phys. 33, 2716 (1962).

5. W. P. Mason and A. Rosenberg, "Phonon and Electron Drag Coefficients in Single Crystal Aluminum," Phy. Rev. 151, 434 (1966).

6. R. W. Guard, "Rate Sensitivity and Dislocation Velocity in Silicon Iron," Acta Met. 9, 163 (1961).

7. D. F. Stein and J. R. Low, Jr., "Mobility of Edge Dislocations in Silicon-Iron Crystals," J. Appl. Phys. 31, 362 (1960).

8. R. C. Blish III, "Dislocation Velocity and Slip on the $\{\bar{1}2\bar{1}2\}\langle 1\bar{2}13\rangle$ Systems of Zinc," Ph.D. Thesis, California Institute of Technology, Pasadena, California (1967).

9. R. W. Rohde and C. H. Pitt, "Dislocation Velocities in Nickel Single Crystals," J. Appl. Phys. 38, 876 (1967)

10. W. F. Greenman, "Dislocation Mobility in Pure Copper Single Crystals," Ph.D. Thesis, California Institute of Technology, Pasadena, California (1966).

11. K. Marukawa, "Dislocation Motion in Copper Single Crystals," J. Phys. Soc. Japan 22, 499 (1967)

12. T. Suzuki, "Dislocation Motion and Yield Stress in Pure Copper and its Dilute Alloy," to be included in the report of the Battelle Colloquium on Dislocation Dynamics held at Harrison Hot Springs, Canada, May 1967; to be published by McGraw-Hill.

13. T. Suzuki and T. Ishii, "Dislocation Motion and Yield Stress in Copper-Nickel Dilute Alloys at Low Temperatures," to be published in the Proceedings of the International Conference on the Strength of Metals and Alloys, Tokyo, Sept. 1967.

14. T. Suzuki and H. Kojima, "Dislocation Motion in Silicon Crystals as Measured by the Lang X-Ray Technique," Acta. Met. 14, 913 (1966).

15. D. P. Pope, "The Mobility of Edge Dislocations in the Basal Slip System of Zinc," Ph.D. Thesis, California Institute of Technology, Pasadena, California (1967).

16. D. P. Pope, research in progress, W. M. Keck Laboratory of Engineering Materials, California Institute of Technology, Pasadena, California.

17. J. Friedel, Dislocations, Pergamon Press, Ltd., London (1964), p. 158.

18. K. Jassby, research in progress, W. M. Keck Laboratory of Engineering Materials, California Institute of Technology, Pasadena, California.

19. F. W. Young and J. R. Savage, "Growth of Copper Crystals of Low Dislocation Density," J. Appl. Phy. 35, 1917 (1964).

20. T. S. Noggle, "A 'Soft' Mold Technique for Growing Single Crystals of Aluminum," Rev. Sci. Instr. 24, 184 (1953).

21. A. P. L. Turner, T. Vreeland, Jr., and D. P. Pope, "Experimental Techniques for Observing Dislocations by the Berg-Barrett Method," accepted for publication by Acta Cryst.

22. D. P. Pope, T. Vreeland, Jr. and D. S. Wood, "Machine for Producing Square Torsion Pulses of Microsecond Duration," Rev. Sci. Instr. 35, 1351 (1964).

23. J. Friedel, Dislocations, Pergamon Press Ltd., London (1964), p. 31 and 65.

24. W. G. Ferguson, A. Kumar, and J. E. Dorn, "Dislocation Damping in Aluminum at High Strain Rates," J. Appl. Phys. 38, 1863(1967).

25. J. J. Gilman, "Dislocation Mobility in Crystals," J. Appl. Phys. 36, 3195 (1965).

26. R. L. Fleischer, "Rapid Solution Hardening, Dislocation Mobility, and the Flow Stress of Crystals," *J. Appl. Phys.* *33*, 3504 (1962).

27. J. E. Dorn and S. Rajnak, "Nucleation of Kink Pairs and the Peierls Mechanism of Plastic Deformation," *Trans. AIME* *230*, 1052 (1964).

28. A. Seeger, S. Mader, and H. Kronmüller, "Theory of Work Hardening of FCC and HCP Single Crystals," *Electron Microscopy and Strength of Crystals*, Interscience Publ., New York (1963), p. 665.

29. W. P. Mason, "Phonon Viscosity and Its Effect on Acoustic Wave Attenuation and Dislocation Motion," *J. Acoust. Soc. Am.* *32*, 458 (1960).

30. W. P. Mason and T. B. Bateman, "Ultrasonic-Wave Propagation in Pure Silicon and Germanium," *J. Acoust. Soc. Am.* *36*, 644 (1964).

31. W. P. Mason, "Drag on Dislocations Due to Thermal Losses of the Phonon-Phonon Interaction Type," *J. Appl. Phys.* *35*, 2779 (1964).

32. J. Lothe, "Theory of Dislocation Mobility in Pure Slip," *J. Appl. Phys.* *33*, 2116 (1962).

33. W. P. Mason, *Physical Acoustics and the Properties of Solids*, D. Van Nostrand Co. (1958), p. 323.

34. W. P. Mason, "Mechanism for Electron Damping of Dislocations in Pb," *Appl. Phys. Letters* *6*, 111 (1965).

35. J. J. Gilman, "Dislocation Motion in a Viscous Medium," *Phys. Rev. Letters* *20*, 157 (1968).

36. J. D. Eshelby, "Dislocations as a Cause of Mechanical Damping in Metals," *Proc. Roy. Soc.* *A197*, 396 (1949).

37. J. H. Weiner, "Thermoelastic Dissipation Due to High-Speed Dislocations," *J. Appl. Phys.* *29*, 1305 (1958).

38. G. Leibfried, "Uber den Einfluss Thermisch Angeregter Schallwellen auf die Plastische Deformation," *Z. Phys.* *127*, 344 (1950).

39. F. R. N. Nabarro, "The Interactions of Screw Dislocations and Sound Waves," *Proc. Roy. Soc.* *A209*, 278 (1951).

40. J. D. Eshelby, "The Interaction of Kinks and Elastic Waves," *Proc. Roy. Soc.* *A266*, 222 (1962).

41. J. Lothe, "Aspects of the Theories of Dislocation Mobility and Internal Friction," Phys. Rev. 117, 704 (1960).

42. R. Hill, Plasticity, Oxford University Press, London (1950), p. 89.

43. D. S. Wood, private communication (1968).